Utah State University

DigitalCommons@USU

5-2016

Frictional Heating of Fault Surfaces Due to Seismic Slip: Experimental Studies on the Hematite to Magnetite Transition and Federal and Private Landownership's Effect on Oil and Gas Drilling and Production in the Southwestern Wyoming Checkerboard

David W. Jenkins
Utah State University

Follow this and additional works at: https://digitalcommons.usu.edu/gradreports

Utah State University
MERRILL-CAZIER LIBRARY

Frictional Heating of Fault Surfaces Due to Seismic Slip: Experimental Studies on the
Hematite to Magnetite Transition

and

Federal and Private Landownership's Effect on Oil and Gas Drilling and Production in the
Southwestern Wyoming Checkerboard

by

David W. Jenkins

A report submitted in partial fulfillment of the requirements for the degree

of

Master's of Science

in

Applied Environmental Geoscience

Approved:

_____   _____

Dr. James P. Evans   Dr. Kelly Keighley Bradbury
Major Professor   Committee Member

_____

Dr. Alexis K. Ault
Committee Member

Utah State University
Logan, Utah

2016

PUBLIC ABSTRACT

Frictional Heating of Fault Surfaces Due to Seismic Slip: Experimental Studies
on the Hematite to Magnetite Transition

And

Federal and Private Landownership's effect on Oil and Gas Drilling and
Production in the Southwestern Wyoming Checkerboard

by

David W. Jenkins, Master's of Science

Utah State University, 2016

Major Professor: Dr. James P. Evans
Department: Geology

This report is a two-part presentation of research within in the fields of rock mechanics and natural resource economics. The first chapter addresses the use of iron oxide oxidation state and thus mineral transitions as a method for determining the frictional temperature rise achieved during an earthquake. Experimental literature on the hematite to magnetite transition is reviewed. Magnetite from transformed or reacted hematite forms between 300-1240 °C. Design and experimental results for a rotary shear apparatus in which hematite is deformed are reported. The measured coefficient of friction for synthetic hematite gouge is 0.38 ±0.03. The second chapter is an investigation of oil and gas production outcomes between federal and private land using a randomized treatment of land ownership. The data comprises oil and gas well drilling and production records located in the railroad land checkerboard, southwestern Wyoming. Spatial and graphical analysis of production and drilling records reveal that federal mineral leases are developed systemically later than private land.

DEDICATION

I dedicate this work to my beautiful wife Chelsie, sweet little girl Maggie, and little buddy

Mason.

ACKNOWLEDGMENTS

CONTENTS

LIST OF FIGURES

LIST OF TABLES

CHAPTER 1

Frictional Heating of Fault Surfaces Due to Seismic Slip: Experimental Studies on the Hematite to Magnetite Transition

ABSTRACT

This project serves as a literature review on the transformation and synthesis of magnetite from hematite under hydrothermal conditions as well as with Pulsed Laser Deposition (PLD) and milling. Magnetite forms over a similar range of elevated temperatures regardless the method that is used to synthesize it, including non-heterogeneous, loosely controlled environments such as a ceramics kiln. Based on these experiments, magnetite on a fault surface created from the high temperature reduction of Fe during seismic slip may indicate the fault experienced temperatures between 300 - 1240°C. Duration of seismic slip is short, therefore, in order for magnetite to develop in any appreciable quantities optimal conditions for magnetite formation must be reached. Ideal conditions for magnetite formation are low fO_2, high normal loads, and temperatures of at least 450 - 475°C in a non-equilibrium environment.

A rotary shear apparatus was constructed to investigate the impact of frictional heating of hematite gouge by determining the coefficient of friction of hematite experimentally. Twelve experiments over normal loads of 15 – 70 MPa reveal that the mean experimental coefficient of friction of hematite is 0.38 ± 0.03. A detailed description of the apparatus and its operating procedure are discussed. Results of rotary shear are used to inform existing thermodynamic models and to approximate temperatures during slip of iron oxide coated faults.

INTRODUCTION

Determining the peak temperature of a fault surface during slip sets important rheologic constraints on the upper limits of the seismogenic zone. There are few direct indicators of maximum frictional heat on a fault surface other than presence of frictional melt (Cowan, 1999) or changes to organic biomarkers (Savage et al., 2014). For example, Savage et al. (2014) used the transformation of biological markers to indicate that fault temperature rise was 800-1170°C above the ambient temperature in a pseudotachylyte bearing fault. Evans et al. (2014) reported iron oxide phase changes on the Wasatch Fault, near Willard, Utah, and suggest the transition is caused by frictional heating due to earthquake nucleation in the brittle regime. These observations, and those of Ault et al. (2015), and McDermott et al., (2015), suggest that understanding the possible reduction of hematite caused by elevated temperatures will help constrain the rock properties that determine earthquake parameters. In addition, examining the transformation of Fe oxide bearing minerals is attractive as iron is common in fault zones, and there are a range of experiments and analytical methods that can be used to investigate iron in rocks.

The purpose of this report is to review the potential of iron oxide phase transitions as a temperature indicator on natural fault surfaces. This was accomplished by exploring experimental literature in which hematite (Fe_2O_3) has been experimentally transformed to magnetite ($FeO\text{-}Fe_2O_3$). The design and construction of a rotary apparatus is discussed, and experimental data that report the coefficient of friction for hematite will be presented. Results from analysis of iron oxides in kiln fired ceramic glazes are also reported and discussed. Reviewed iron oxide studies to be presented are from the geochemical and material sciences focusing both on equilibrium and non-equilibrium processes.

Experimental data is reported that delineate the detection limits of magnetite from X-Ray Diffraction (XRD). These techniques comprise a relative standard from which results from rotary shear of hematite gouge and firing of iron oxides in ceramic glazes will be compared.

BACKGROUND

Frictional heating that occurs during active faulting is explored and described with modeling (Sibson, 1975; Lachenbruch, 1980, 1986; O'Hara, 2005; Rempel and Rice, 2006), experimental studies(Di Toro et al., 2011; Goldsby and Tullis, 2011; Noda et al., 2011; Fondriest et al., 2013), and textural analysis of natural faulted materials (Spray, 1992; Evans et al., 2014; Prante et al., 2014; Savage et al., 2014; Ault et al., 2015), among many other studies. Previous researchers have primarily focused on frictional temperature rise via seismic slip as it relates to pseudotachylyte formation or fault melt (Sibson, 1975; Spray, 1992; O'Hara, 2005; Rempel and Rice, 2006).

Thermal processes important in a fault zone can be divided into four categories (Rice, 2015): 1. Shear heating, 2. Asperity (Flash) heating, 3. Transformation –reaction heating, and 4. Melting. In nature the manifestations of these mechanisms are difficult to interpret (Takacs 1998, 2002). Shear heating associated with pseudotachylyte generation was conceptualized by Sibson (1975) and proposed as a driving mechanism for thermal pressurization of faults to reduce the effective normal stress. Lachenbruch (1986, 1980) further modeled the concept of shear heating and its effect on fault geometry and its development in space. Asperity (flash) heating, caused by the Joule-Thompson effect resulting from adiabatic decompression of asperities as proposed by O'Hara (2005) helps explain additional heat generated during seismic slip. Chemical interaction of minerals that are comminuted to nanoparticle size during slip can react exothermically and also result in high localized heat along fault surfaces (Rice, 2015). Both shear and flash heating cause reactions above their activation energy (Takacs, 1998; Yetter et al., 2009).

PREVIOUS WORK

Wasatch Fault Damage Zone, Willard Utah

Observations by Evans and Langrock (1994), Evans et al. (2014), Ault et al. (2015), and McDermott et al. (2015) of the Wasatch Fault damage zone between the Willard and Brigham City segment in Willard, UT, small fault surfaces with areas on the order of centimeters of slip covered in thin red to purple hematite coatings and exhibit a high degree of luster. These ≤ mm-thick high gloss surfaces are black, mirror like, and/or contain iridescent patches that resemble 'blued steel' (Evans and Langrock, 1994). Further work by Ault et al. (2015) and McDermott et al. (2015) indicate that similar faults are observed elsewhere. A key piece of evidence that these high-gloss surfaces are created by seismicity is that reduced Fe, presumable in the form of magnetite is present in the iridescent patches. Reduction of Fe^{3+} in hematite to Fe^{2+} requires substantial heat or a highly reduced environment (Frost 1991). Evans et al. (2014) used X-ray photo-electron spectroscopy (XPS) to analyze the iridescent patches on the small fault surfaces and a best fit model for the data was created. The best-fit model showed 30% Fe^{2+} and 70% Fe^{3+} in the iridescent patches. A gauss-meter was used to characterize surfaces as well and 320mG variations (characteristic of magnetite) in magnetization were recorded in the iridescent zones (Evans et al., 2014). When these surfaces are viewed with Scanning Electron Microscopy (SEM), the hematite grains are highly comminuted and are submicron in size (Ault et al., 2015). Adjacent to the fault surface and associated with iridescent regions are 300-500 μm in diameter polygonal Fe oxides crystals (Ault et al., 2015). This texture is interpreted to reflect annealing from flash heating (Ault et al., 2015). Magnetite crystals must be even smaller and have not been identified with an SEM (Evans et al., 2014; Ault et al., 2015). Further analysis

using X-ray Near Edge Spectroscopy (XANES) confirms the presence of reduced Fe on the

fault surface for the Wasatch Fault and on subsidiary fault surfaces within the southern San

Andreas Fault system in the Mecca Hills, California (Evans personal communication 2016).
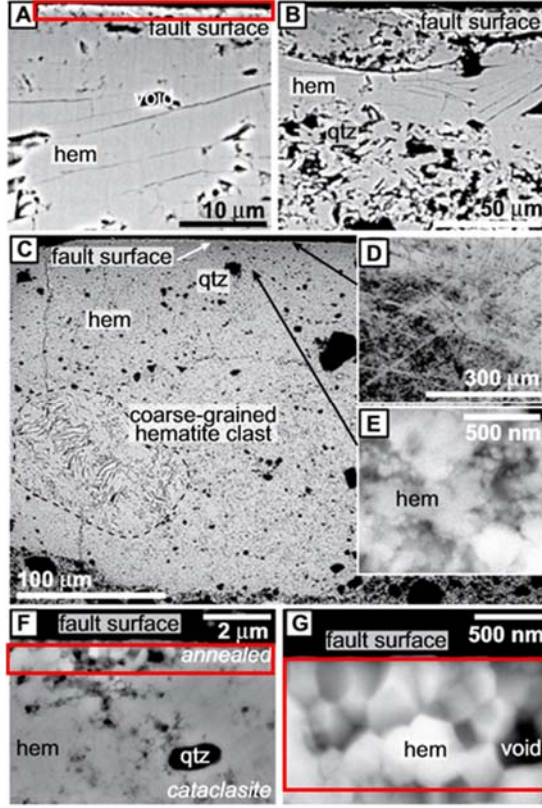
Figure 1. Hematite microtextures. "Hematite fault surface micro-structural observations from backscattered electron images. A, B: Sample A13-3 cross-sectional images with hematite (hem) plates (qtz—quartz). C: Sample WF94-17 cross-sectional image with hematite cataclasite, coarser-grained hematite clast, lesser sub-angular quartz grains, and contact with host rock. D: Associated fault surface image with multiple slickenline orientations. E: Detail of sample WF94-17 hematite cataclasite with subangular to subrounded crystals. F: Polygonal hematite crystals are located within 2 mm of slipsurface with cataclasite below. G: Closeup example of F." [figure, annotations, and description directly from Ault et al., (2015) with bolding of fonts added as well as figure designation].

Boxed in red are polygonal crystals that have been associated with annealing.

The temperature rise for slip along a fault is calculated as:

$$\Delta T = \alpha \mu \sigma_{ne} v \sqrt{\frac{1}{\frac{\kappa}{l_t}}} \tag{1}$$

where ΔT is the change in temperature in Kelvin, μ is a coefficient of friction, σ is normal

stress on the effective slip surface, ν is the slip velocity, ϰ is the heat capacity, l_t is the thermal

diffusive length into the wall rock, and α is an asperity shape constant. Evans et al. (2014)

made the following assumptions: A constant slip velocity of 1m/sec, 1-10mm circular

asperities, heat capacity of 1 Joule/(mol*K), 40 MPa of normal stress, 1μm diffusive length,

and a coefficient of friction equal to 0.6 (Ashby et al., 1991; O'Hara, 2005; Beeler et al., 2008, 2008; Evans et al., 2014).

A temperature >300 °C can be expected along the fault plane using the nominal values from Evans et al. (2014) and thereby explain flash heating and transformation of hematite to magnetite.

Ault et al. (2015) further described the same surfaces mentioned in Evans et al. (2014) using Backscatter Electron Microscopy (BSE). Polygonal crystals are located within 2μm of the fault surface and serve as textural evidence that at the fault interface, flash heating occurred (Ault et al., 2015). This inference is explained by adiabatic heating from rapid decompression of an asperity as being >800 °C (O'Hara, 2005). Ault et al. (2015) suggests that annealing textures seen adjacent to the principal slip surface hematite formed between 800 – 1000 °C and seems to exhibit this same polygonal texture as natural hematite found on at the interface of highly polished slip surfaces (Vallina et al., 2014).

Review of Previous Work: Hematite to Magnetite Transitions

Hydrothermal Synthesis of Magnetite

Equilibrium hydrothermal laboratory experiments report the oxidation and reduction of iron Fe^0, Fe^{2+}, and Fe^{3+} to form magnetite in a rigorous and quantitative manner (Matthews, 1976; Cole et al., 2004; Otake et al., 2010; Solferino and Anderson, 2012). Each of the four experiments presented lend insight to the optimal temperatures in which magnetite formed under equilibrium conditions.

Oxygen fugacity (fO_2) or the partial pressure of oxygen, is an important variable in each experiment, because iron exists in three valences and will behave differently under unique temperature - fO_2 conditions (Fig 3). Oxygen fugacity can be thought of as the activity of oxygen (Frost, 1991). Strict control of fO_2 in the experimental apparatus is usually accomplished by using a buffer such as the Ni-NiO buffer, or limiting the amount of O_2 in the system by vacuum/inert gas flush (Lindsley, 1991). Temperature, pressure, and fO_2 will control the formation of iron oxide minerals and their metastable phases (Frost, 1991).
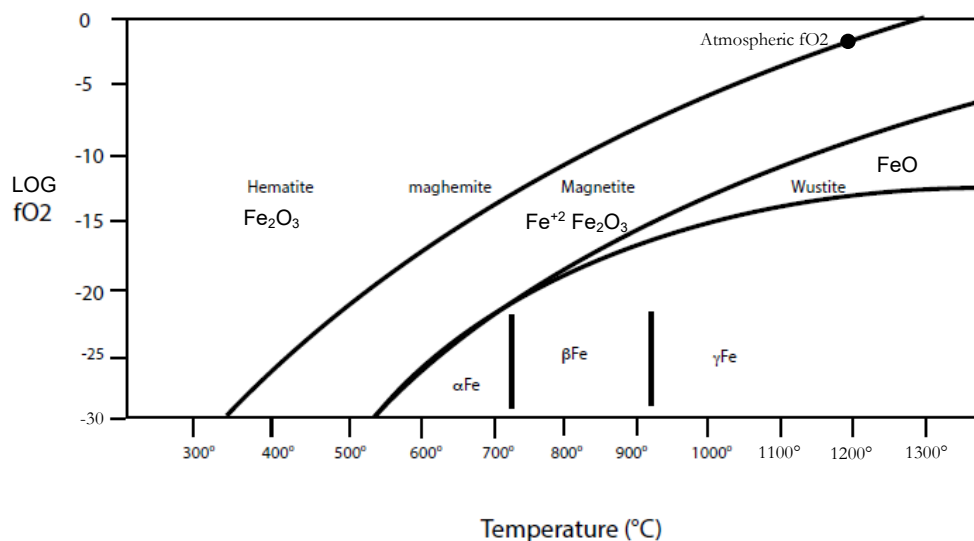
Figure 2. Phase diagram of the iron oxide system. Plotted as temperature (°C) vs oxygen fugacity (fO2). Modified from Essene and Fisher (1986).

Matthews (1976) studied the formation of magnetite under hydrothermal conditions by reacting hematite with non-valent iron between temperatures of 350-570°C and pressures of 1-2 Kbars. Oxygen fugacity is controlled for by use of a Ni-NiO buffer. Reactions between elemental Fe and hematite occur as a non-stoichiometric redox reaction in two steps with variable rates. Reactions proceed to completion in ~0.25 hrs when powdered elemental iron is reacted with powdered hematite in water. For temperatures ≥555°C only magnetite can be detected (Matthews, 1976).

Cole et al. (2004) investigated the oxygen fractionation in magnetite in isotopically different waters to better constrain the magnetite-water geothermometer. Hematite to magnetite hydrothermal experiments were performed from 300-800°C and at pressures of 10-215MPa (Cole et al., 2004). Quantitative X-ray diffraction (XRD) determined the mol percent magnetite yield. Optimal magnetite creation of magnetite was between 335-350°C when hematite is heated in the presence of 0.5M acetic acid. Temperature, pressure, and

starting material were found to impact the extent of crystallization, grain size, and crystal habit of both magnetite and hematite (Cole et al., 2004).

Solferino and Anderson (2012) performed experiments under higher pressures up to ~136 MPa using a diamond anvil cell apparatus with a N_2 flush to control fO_2. The optimal formation temperature for magnetite with their given conditions was 490-500°C.

Otake et al., (2010) reacted hematite and magnetite with acid under hydrothermal conditions as well as performed acid base titrations. The partial pressure of H_2 was raised from 0.05-5 MPa during experiments at temperatures from 100-250°C. Non-redox behavior controlled the reactions for the first 1-3days depending on the temperature. Constants for the non-redox reactions were then determined from acid base titrations (Otake et al., 2010).

Equilibrium Hydrothermal Experiments					
Study	fO$_2$ Control	Pressure	T° Range	Optimal T° for Magnetite	Time
Cole 2004	Vacuum Oven	100 Mpa	300 - 800°C	**350°C**	N/R
Otake 2010	H$_2$ and Ar Flush	Not reported	100 - 250°C	**Not Reported**	NR
Matthews 1976	Ni / NiO Buffer	100 MPa	350 - 570°C	**555°C**	0.25 hrs
Solferino 2012	N$_2$ Flush	97.4 - 136.3 MPa	475 - 500°C	**490 - 500°C**	NR

Table 1. Experimental results of the hydrothermal synthesis of magnetite. Controls on the experiments such as oxygen fugacity, pressure, and temperature range are listed. Optimal conditions found in each experiment are also noted. Not reported (NR)

Pulsed Laser Deposition of Magnetite Films

Pulsed Laser Deposition (PLD) is a method used by the nano-materials community for synthesizing magnetite films and is a non-equilibrium process that allows environmental factors to be controlled while varying temperature that is (Shima et al., 2002).
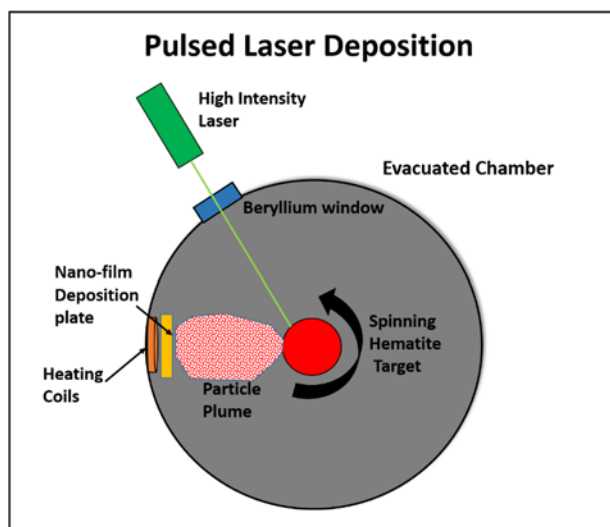
Figure 3. Schematic of Pulsed Laser Deposition in plan view. A high intensity laser impacts a spinning hematite target inside an evacuated chamber. A plume of hematite nanoparticles are formed from coulomb explosion (Hashida et al. 2009) caused by the laser. Hematite nanoparticles collect on an inert substrate (Si, MgO, ect.) that is heated to a background temperature. (schematic created from descriptions of PLD(Shima et al., 2002; Tepper et al., 2004; Tiwari et al., 2009; Sanz et al., 2013))

The percent yield of magnetite and its crystal structure are controlled by the background temperature of the substrate during deposition (Shima et al., 2002; Tepper et al., 2004; Tiwari et al., 2009; Sanz et al., 2013). Magnetite formation using PLD also changes when fO_2 is varied (Guo et al., 2013). For instance, if the same laser settings are used to ablate a hematite target in a reduced environment, a maghemite film will form rather than a hematite film (Shima et al., 2002). Table 2 contains the relevant methods and results of magnetite formation from notable PLD experiments with respect to magnetite.

Non-equilibrium Pulsed Laser Deposition of Magnetite Films				
Study	**P_{O2}**	**Laser Settings**	**T° Range**	**Optimal T° for Magnetite**
Shima 2002	6×10^{-2} Pa	250 - 550 mJ 20 Hz	25 - 500°C	**400°C (maghemite and magnetite)**
Tiwari 2009	2×10^{-2} Pa	9 mW 10 Hz	350 - 550°C	**450°C (magnetite)**
Tepper 2004	1×10^{-2} Pa	300 mJ 5 Hz	500°C	**No Variation in Temperature**
Sanz 2013	2×10^{-2} Pa	20 mW 10 Hz	300 - 750°C	**475°C (magnetite)**

Table 2. Experimental results PLD deposition of magnetite films. Contains the partial pressure of oxygen (fO_2), power of laser with its associated wavelength, temperature range at which experiments were run, and optimal temperature of substrate for formation of magnetite films thickness and percent yield of magnetite.

Optimal formation temperatures of magnetite in the PLD experiments closely coincide with those found in the equilibrium hydrothermal experiments. Typical deposition rate for magnetite films is ~10 μg/(cm^2 min). The power and pulse frequency of the laser are potential contributing factor of magnetite formation, assuming magnetite instantly forms upon photon impact. Unfortunately, it is difficult to measure the temperature directly when the laser impacts the substrate. What is known, however, is that when the same laser settings are used to ablate a hematite target, the background temperature of the deposition plate controls the formation of either a hematite, maghemite, or magnetite film (Sanz et al., 2013).

Ball-milling

Ball-milling is considered a "brute force chemistry" method, where reactants are forced together in order to produce steel and other metal alloys in a non-equilibrium environment. Powders reacted together within the ball-mill are mechanically activated via plastic deformation transforming a portion of the kinetic energy into heat (Suryanarayana, 2001). Variables such as oxygen fugacity, grain size reduction, milling temperature, and total system energy are set at a constant rate. Reactions and phase changes in nano-particles are observable and measureable because the ball-mill can be stopped and sampled at any point in time (Suryanarayana, 2001).

The transition of Fe^{3+} in hematite to Fe^{2+} in magnetite is hypothesized to be evidence of seismic slip on a fault surface (Evans et al., 2014). The purpose of this portion of the review is to report experimental results from ball-milling hematite powder. In these

experiments, Fe^{3+} is transformed to Fe^{2+} in magnetite owing to elevated temperatures under particular conditions.

How mechanical alloying and milling work

Ball-mills come in various styles (Fig. 4) but operate on the same principles. A drum is rotated with a grinding medium and a substrate to be mechanically alloyed or milled. The grinding medium (balls), vary in size and material depending on the substrate being used. Substrate, typically a powder, is impacted between two or more grinding media and is deformed by both brittle and plastic mechanisms (Fig. 5). Brittle deformation serves to reduce grain size and plastic deformation compacts and reacts the substrate.

The variables that are important to the milling process are: 1) type of mill and its dimensions; 2) milling energy and speed; 3) length of time powder is milled; 4) grinding medium type, size, and size distribution; 5) ball-to-powder weight ratio; 6) extent of vial filling; 7) composition of milling atmosphere; 8) catalysts used; and 9) milling temperature (Suryanarayana, 2001). Hereafter, I focus on the milling temperature.

Temperature rise during milling

Temperature rise during milling occurs due to friction and adiabatic decompression from impact of grinding balls with the cylinder, with other grinding balls, and/or substrate. The two types of temperature rise of interest are: 1) the overall rise in temperature, and 2) the discreet temperature rise on impact. Overall temperature rise is modeled by the *Equation 2* and discreet temperature rise by *Equations* **3 and 4**.

Device	Simoloyer®	Planetary Ball Mill	Attritor®	Drum (ball) mill
Maximum diameter [m]	0.9	0.2	1	3
Maximum total volume [l]	400	8	1000	20000
Maximum relative velocity [m/s]	14	5	4.5 - 5.1	< 5
Graphic (cross section)				

Simoloyer® is a brand of Zoz GmbH, Germany; Attritor® is a brand of Union Process, USA;
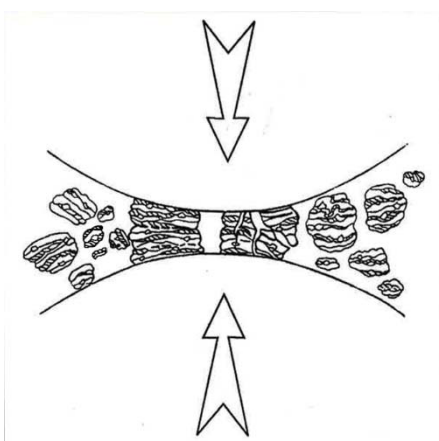
Figure 4. (Above) Various types of ball-mill and **specifications** (Suryanarayana, 2001).

Figure 5. (Left) Cross-section of grinding balls colliding and deforming substrate. (Suryanarayana, 2001).
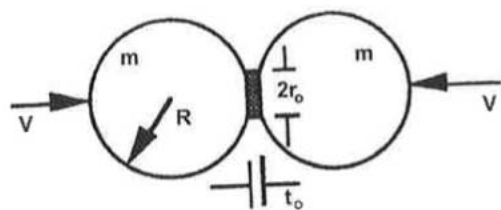
Figure 6. Schematic of milling variables. Eqn. 2. Describes maximum discreet temperature rise when two grinding balls impact substrate (Suryanarayana, 2001)

$$\Delta T = J\sqrt{\frac{\Delta t}{\pi \kappa \rho c}} \tag{2}$$

$$\Delta T = \frac{2q_2\Delta t}{\rho c t_0} + \frac{q_2 t_0}{2\kappa}\left[\frac{1}{3} - \frac{2}{\pi^2}\sum_{n=1}^{\infty}\frac{(-1)^n}{n^2}\exp\left(-\frac{4n^2\alpha\Delta t}{t_0^2}\right)\cos(n\pi)\right] \tag{3}$$

Where

$$q_2 = \frac{\delta Q}{\pi r_0^2 \Delta t} \tag{4}$$

Where ΔT is the maximum overall temperature rise, $J = \sigma_n v_r$ is the energy flux where σ_n is the normal stress and v_r is the relative velocity of grinding media. The value Δt is duration of milling, and $\kappa \rho c$ are thermal conductivity, density, and specific heat capacity of the powder respectively (Schwarz and Koch, 1986).

Equations 3 and 4 model the maximum temperature rise of single collisions. ΔT is the maximum temperature rise for a single collision assuming all heat is from adiabatic decompression. Q is the average quantity of heat (derived from eqn. 1), δ is the fraction of heat flowing into the powder, r_0^2 is the width of the compact powder (see Fig. 6), t_0 is the thickness of the powder compact cylinder, and α is the thermal diffusivity (Bhattacharya and Arzt, 1992). The other variables are same as stated above. Discreet temperature rise from impact has not been validated because it occurs within 10^{-5}s so the classical thermodynamic model of *Equations 3 and 4* are the best approximation thus far.

Ball mill transformation of hematite to magnetite

Betancur et al. (2003) used a planetary ball-mill under a high flow of N_2 and H_2 gas to transform hematite to magnetite. Distilled water was added to pure hematite in an evacuated stainless steel planetary ball-mill. The ball to powder ratio was 1 to 30 and the ball mill was rotated at 280rpm. Mössbauer spectroscopy and X-ray diffraction (XRD) were used to characterize the change with increased time. It was found that increased milling time resulted in a higher yield of magnetite (*Fig. 7*). After 12.5 min of milling only magnetite could be detected. In a similar study done by Campbell et al., (1995) average crystallite size of magnetite and hematite was reduced to 30nm; however, the size of starting material is not reported. Temperature rise of the milling vial as well as theoretical calculation of heat generated in discreet ball to powder impacts are not reported.

Sakthivel et al. (2014) also used a planetary ball-mill to cause the hematite-magnetite transition but did so in the presence of highly reactive elemental iron. A metastable wüstite phase was observed after 10hrs of milling.
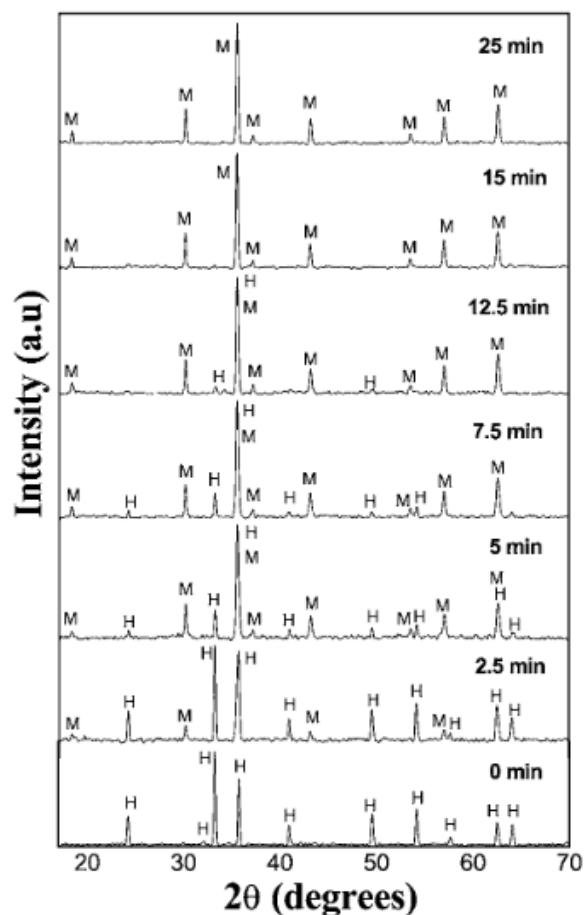
Figure 7. XRD spectra with increased milling time. Magnetite peaks (M) and hematite peaks (H). Note that the large peak at ~35° is shared by M and H (Betancur et al., 2003).

Iridescent ceramic glazes

Ancient Chinese ceramics known as "black Jian tea bowls" provide natural experiments in iron oxide transformation (Dejoie et al., 2014). Potters collected iron rich clay from the countryside and made bowls and teacups. Wares were then fired, creating unique textures as well as iridescence (Li et al., 2008).

Dejoie et al. (2014) analyzed glaze from these bowls with SEM, Transmission Electron Microscopy (TEM), and XRD. Pottery glaze was found to contain significant amounts of magnetite and a metastable form of iron oxide (ϵ-Fe_2O_3). Magnetite and ϵ-Fe_2O_3 formation is attributed to thermal reduction during the firing process. Thermal reduction of the wares fired in open air occur at 1240°C (Li et al., 2008).

Matt Fiske is currently reproducing iron oxide rich glazed textures as part of his Masters of Fine Arts at Utah State University. His pottery us glazed using pulverized iron rich basalts and subjected to a reducing kiln. Fe^{3+} in iron oxides is thermally reduced creating similar textures to those found in ancient Chinese pottery (Fig. 8). Typically iridescence is produced when these glazes are fired at 1230°C.

Figure 8. Ceramic work by M. Fiske (left). Base glaze substrate to (right). Glaze created from 25% basalt and 75% rhyolite.

SUMMARY OF LITERATURE REVIEW

Results from equilibrium hydrothermal and non-equilibrium ball-milling experiments demonstrate that hematite is completely transformed to magnetite in ~15 min under optimal conditions (Matthews, 1976; Betancur et al., 2003). Magnetite forms readily from hematite in more reducing environments, higher pressures, and moderate temperatures. Even non-heterogeneous, loosely controlled reducing environments such as a ceramics kiln result in the creation of magnetite under high temperatures. Magnetite on a fault surface created from the high temperature reduction of hematite during seismic slip indicates the fault experienced temperatures in the range of 300 - 1240°C. Duration of seismic slip is short, therefore, in order for magnetite to develop in any appreciable quantities optimal conditions for magnetite formation must be reached. Ideal conditions for magnetite formation are low fO_2, high normal loads, and temperatures 450 - 475°C in a non-equilibrium environment.

RESEARCH PROJECT RESULTS

METHODS

X-Ray Diffraction Standard

A standard was created to determine the magnetite detection limits of the X Pert® XRD instrument for pure magnetite/hematite blends (Sigma Aldrich® 99.8% pure). Samples are mixed in known proportions (Table 3) and run at 45 KV/40 mA from 2 - 75° 2θ for 73 minutes. Homogenization of samples was attempted by shaking, but minor clumping of magnetite in samples may have been present. Non-metallic utensils were used to transfer powders. Minor sample separation bias is possible due static electric attraction of plastic and powder. Spectral profiles are then compared to determine when magnetite is measurable (Fig. 9).

Ceramic glazes from M. Fiske were analyzed both before and after firing using XRD. A 25% basalt -75% rhyolite mixture was powdered and heated to 1240°C in a reducing kiln for ~15 minutes. XRD of the glaze powders were performed under the same setting as the standards.

XRD Standard: Weight Percents								
Target mol % (Hem/Mag)	95/5		90/10		80/15		80/20	
	Hem	Mag	Hem	Mag	Hem	Mag	Hem	Mag
Boat weight	0.527	0.595	0.546	0.561	0.533	0.552	0.559	0.525
Boat w/sample	2.383	0.738	2.293	0.848	2.126	0.959	2.035	1.054
Sample weight	1.856	0.143	1.747	0.287	1.593	0.407	1.476	0.529
Boat after	0.546	0.596	0.548	0.561	0.535	0.553	0.565	0.526
Residual left on boat	0.019	0.001	0.002	0	0.002	0.001	0.006	0.001
Sample less residual	1.837	0.142	1.745	0.287	1.591	0.406	1.47	0.528
Actual mol % (Hem/Mag)	94.4/5.6		89.8/10.2		85.0/15.0		80.1/19.9	

Table 3. Mixing percentages for iron oxide. Reports mol pecent of hematite/magnetite after weighing and mixing for XRD. Mol percent is calculated from the stoichiometry of hematite and magnetite.

X-Ray Fluorescence

A Bruker AXS Handheld Inc. S1P X-Ray Fluorescence (XRF) Spectrometer is used to analyze elemental compositions of ceramic glazes before and after firing. Samples are analyzed for 30 seconds at HV ADC 40 in room air optimized for detection of transition metals.

Rotary Shear Apparatus Specifications

Few data exist on the frictional properties of hematite in the rock mechanics literature. Mechanical experiments suggest the coefficient of friction of hematite is 0.60 when ambient temperature is 20°C and decreases to 0.20 at high temperatures (Barrau et al., 2003). Siemes et al. (2003) indicate that crystal plasticity is the dominant deformation mechanism over a wide range of temperatures. To explore the frictional processes that may produce hematite transformations and to estimate the coefficient of friction in hematite, I designed and built a simple rotary shear apparatus. The rotary shear apparatus is housed in a 12 ton (10.886 Kg) shop press with a bottle-jack modified to attach to a 5000 psi (34.5 MPa) hydraulic pressure gauge (Fig. 9). The internal shaft diameter of the bottle-jack is 1.5 inches (38.1mm) with an effective surface area of 1.77 in^2 (11.4 cm^2). The hydraulic pressure gauge has a measurement error of $\pm$ 50 psi (0.34 MPa). The drive mechanism is a one inch steel shaft tapped for a 1.5 inch nut and attached to a two inch chuck for a mini lathe. A rotating ~0.75 inch core or 1 inch bar-stock is secured by three expandable teeth in the lathe chuck (Fig. 10a). A 1 inch diameter packed tapered bearing is seated in a 2 inch diameter port to reduce friction and oppose the normal load of the bottle jack. Stationary core or steel bar-stock is mounted on a 0.25 inch steel plate inside a 2 inch pipe under confining

pressure of another steel pipe tapped for 0.5 inch grubs. The maximum torque is measured with a digital toque adapter with a factory mean calibration error of ± 0.10%.

A granodiorite core sample is used for low normal loads (<15.41MPa), and acts as the wallrock for the experimental fault. The core samples are cut using a 1 inch diamond coring bit which cores to a ~0.75 inch diameter. Copper pipe whose diameter is roughly that of the core was cut used to jacket the core to provide confinement of material. A sample of well-lithified quartz arenite serves as 2 inch diameter stationary base that the rotation core grinds against. Cores were squared to a right cylinder using a diamond saw to ensure a flat surface area for slip.

Steel bar-stock is also used as experimental wall rock, but under high normal loads (7 – 70Mpa) the stationary and rotating core having diameters of 2 inches for the stationary and 1 inch for the rotating. Steel bar-stock is used in place of rock core because we are only interested in the friction properties of the hematite gouge. Pure hematite (Sigma Aldrich® 99.8% pure, <5µm grainsize) is the substrate used for synthetic gouge.

Experimental Procedure

The core sample is secured in lathe chuck as well as stationary sample holder (Fig. 10a). Powdered hematite is placed on the lower rotating core until the angle of repose is met, when compressed, the hematite thickness is 0.0625 inches (1.5mm). Force is increased via the bottle-jack until the desired value is met and held manually during slip. The digital torque adapter and breaker bar is applied until a maximum torque value is reached and static equilibrium is broken. A maximum torque value corresponds to the maximum static coefficient of friction. Pressure is released and the hematite slip surface is inspected visually, removed with clear packaging tape to maintain textural context, and residue is removed with

compressed air. A 350 ft-lb electric impact was used for rotary shear in place of a breaker bar and digital torque adapter, the same procedure applies. Samples from rotary shear friction experiments are not analyzed with XRD because of sample contamination from steel bar-stock and the assumption that the amount of magnetite transformed from hematite would not be greater than 5% or detectable through the XRD method.

We can determine the torque and coefficient of friction for these experiments using:

$$\Gamma = \int_0^{r\,ext} 2\sigma_s r^2 dr = \frac{2\pi\sigma_s r^3}{3} \tag{5}$$

$$\sigma_s = \frac{3\Gamma}{2\pi r^3} = \mu\sigma_n$$

$$\text{or} \tag{6}$$

$$\mu = \frac{\frac{3\Gamma}{2\pi r^3}}{\sigma_n}$$

Where theoretical torque (Γ) can be calculated for two cylinders rotating against each other by knowing the shear force (σ_s) and the radii (r) of the contact surfaces and integrated from r = 0 to r exterior (Di Toro et al., 2010). **Equation 5** can be rearranged to solve for shear force and set equal to resisting forces under static equilibrium conditions. Given this relationship the maximum Γ corresponds to the coefficient of friction (μ) assuming Byerlee conditions.
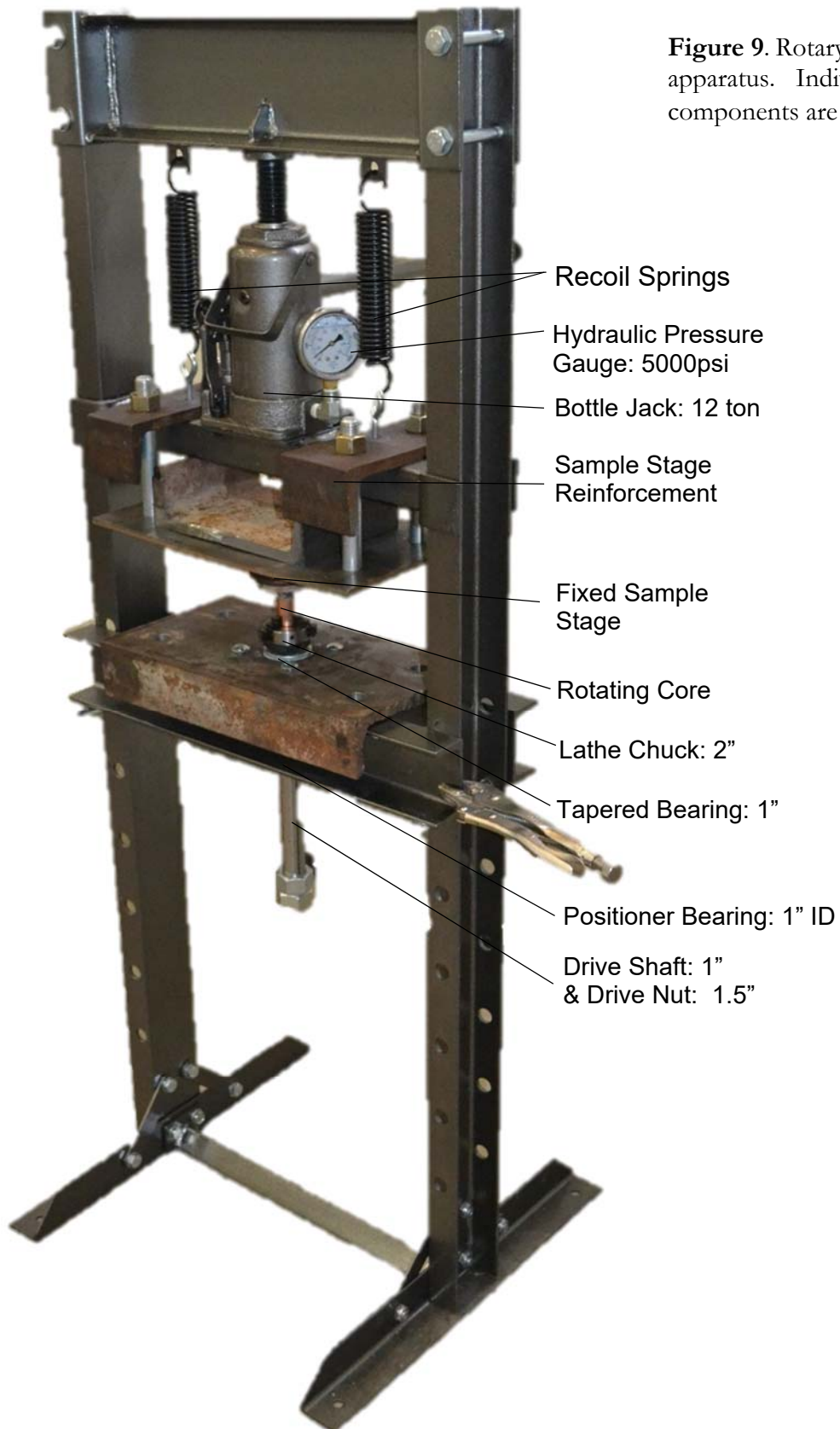
Figure 9. Rotary shear apparatus. Individual components are labeled.

Recoil Springs

Hydraulic Pressure Gauge: 5000psi

Bottle Jack: 12 ton

Sample Stage Reinforcement

Fixed Sample Stage

Rotating Core

Lathe Chuck: 2"

Tapered Bearing: 1"

Positioner Bearing: 1" ID

Drive Shaft: 1"
& Drive Nut: 1.5"

Stationary
Core Holder: 2"

Stationary Core:

Rotating Core:

Copper

Lathe Chuck:

Tapered
Bearing: 1"

Positioner
Bearing: 1" ID

Drive Shaft:

Drive nut: 1.5"
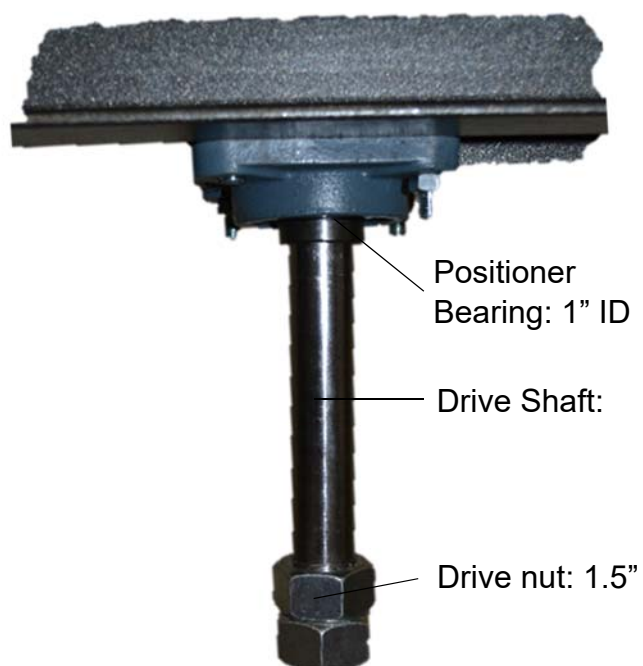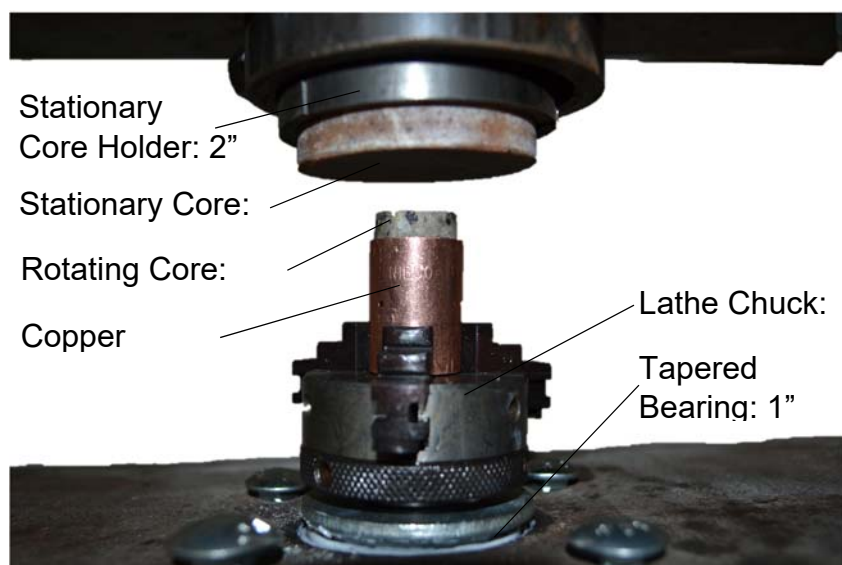
Figure 10. Sample holder and drive mechanism. Sample holder (*above*), upper receptacle grips the stationary core and lower core is contained in a 2" rotating mini lathe chuck. Drive mechanism (*below*) is centered by a positioning bearing and is threaded on both ends.

RESULTS

Results are presented in three categories: the creation of an XRD standard (Fig. 12) for the qualitative comparison and analysis of run products, analysis of ceramic glazes using XRD and XRF (Figs. 13,14), and experimental results of hematite friction and rotary shear experiments (Figs. 11,15,16 and Table 4).

X-Ray Diffraction Standard

XRD intensity profiles vary subtly as mol percent of magnetite is increased relative to hematite (Fig. 12). Magnetite has a diffraction peak at 30° 2θ whereas the main hematite diffraction peak at 49.5° 2θ. Visual inspection of profiles reveal little difference between small mol percent (< 20%) magnetite and the pure hematite profile. X'Pert Highscore® XRD software detects the presence of magnetite between 15 – 20 mol percent relative to other potential minerals.

X-Ray Diffraction and X-Ray Fluorescence of Ceramic Glazes

XRD profiles of glaze before and after firing vary widely (Fig. 12). The glaze prior to firing indicate the existence of quartz, anorthite, clinopyroxene, magnetite, and hematite. After firing a strong SiO_2 peak and broad curved peak is seen in profile between 15° AND 40° 2θ.

Visual inspection of the XRF intensity profiles for glaze before and after firing indicates that the profiles not different. Elemental composition is primarily SiO_2 and Fe (Fig. 13).

Hematite Coefficient of Friction and Rotary Shear

The calculated mean coefficient of friction from measured experimental normal stress and maximum torque is 0.38 (Table 4), with standard deviation of $\pm$ 0.09 and a calculated standard error of $\pm$0.03.   Experiments 2, 3, and 5 yield maximum torques greater than 50% lower than the expected value assuming Byerlee conditions (Byerlee, 1978) and a coefficient of friction of 0.6 (Barrau et al., 2003). Experiments at 2000 and 3000psi were run again to check reproducibility. Difference in coefficients of friction for reproduced runs at gauge measurements of 2000 psi (31.08 MPa) is 0.14 and at 3000 psi (46.62 MPa), 0.04. The coefficient of friction using rock core and hematite gouge is 0.45 (Table 4). Coefficient of friction and the applied normal stress appear to be uncorrelated (Fig. 15).

Granodiorite core fails under normal loads greater than 15.41 MPa with shear, even under the confining stress of copper pipe. Steel bar-stock was then substituted in order to accommodate higher normal loads and shear forces yielding a similar coefficient of friction for hematite gouge.

Hematite gouge exhibited a color change after rotary shear experiments (Fig. 11, 16). After friction experiments a ~2cm wide lighter red hematite compact is left between the two cores with a more granular unconsolidated ring of dark red hematite on the periphery. Small spots dark staining from the steel bar-stock can be seen on the hematite compacts.

Rotary shear of hematite was performed under 46.62 MPa and 350 ft-lbs of hammered toque and resulted in a color change in hematite. Dark metallic fragments from barstock are found

in the residual gouge, but there are also smaller darker particulates whose formation and

origin are not clear.

Figure 11. Stationary quartz sandstone core. Fracture is from failure under uniaxial compression. The hematite gouge is bright red. Core is housed in a notched steel pipe.
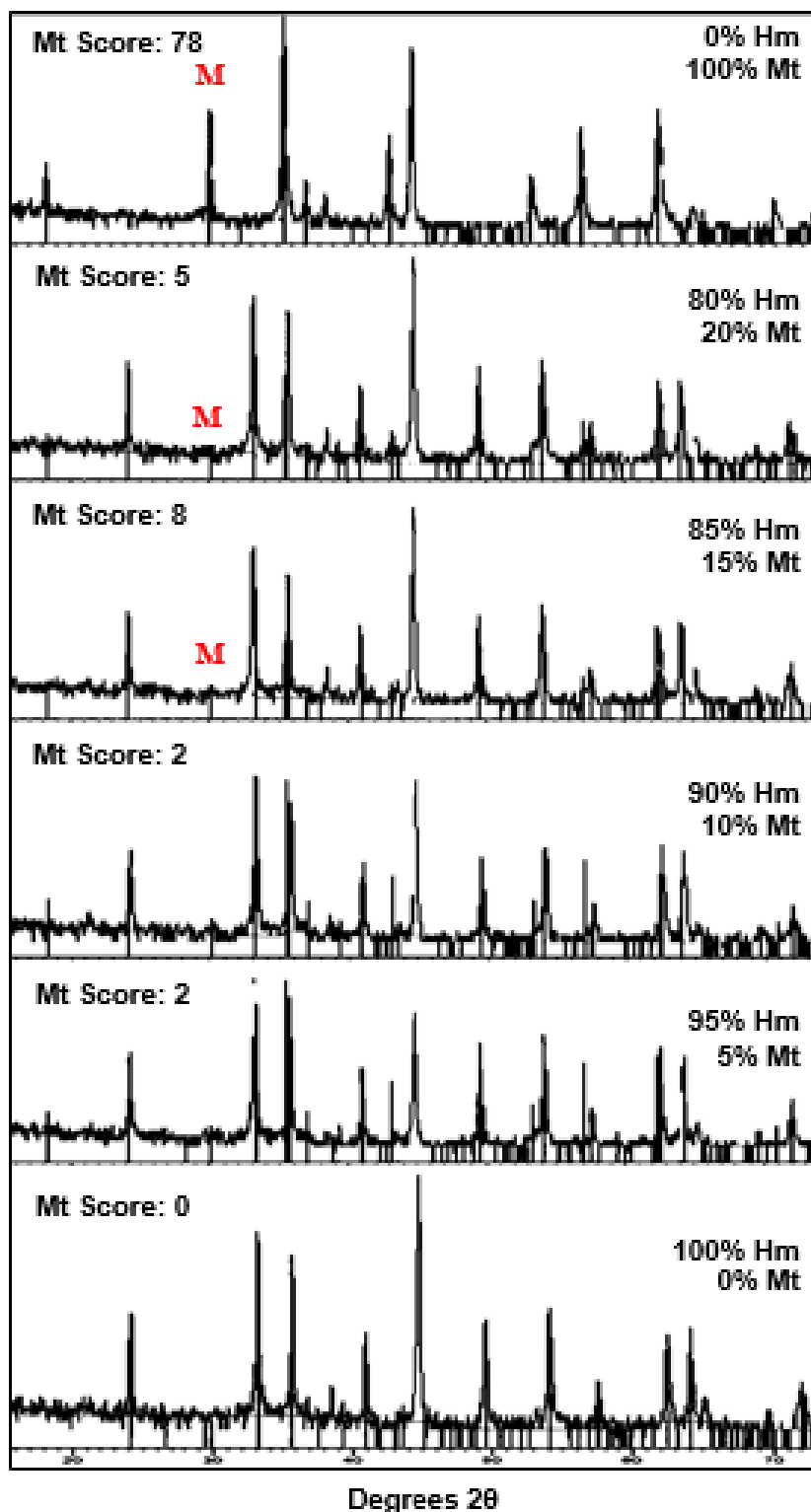
Figure 12. XRD spectra for the hematite/magnetite standard. The vertical axis is peak intensity and the horizontal axis is marked in degrees 2θ. Percentages of hematite and magnetite are to the right with the letter "M" indicating the distinctive 30° 2θ magnetite peak. "Mt score" is a mineral fit ranking ascribed by XRD analysis software. Smaller lines beneath the profile are markers for hematite and magnetite. These profiles omit 0 - 15° 2θ.
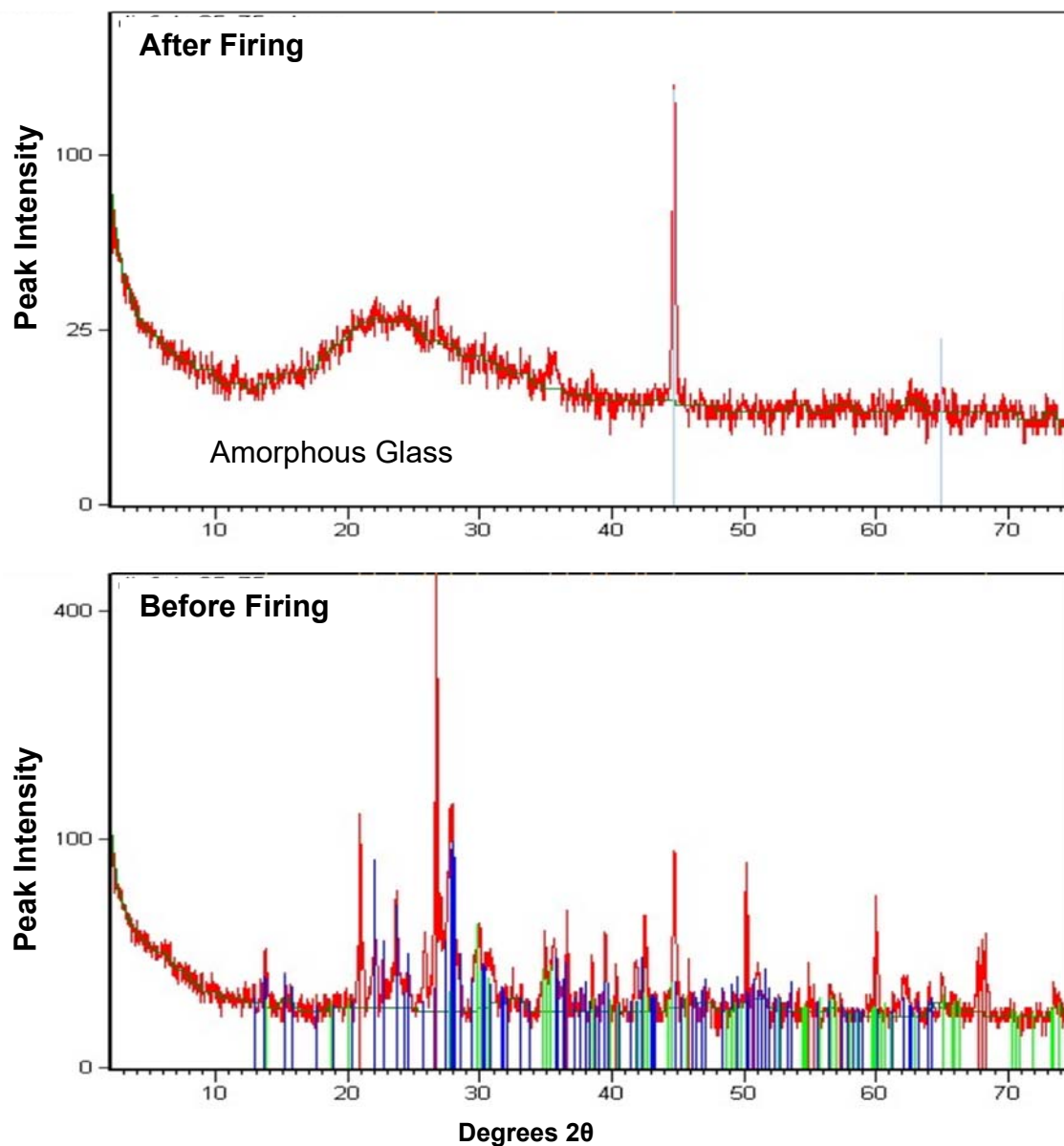
Figure 13. **XRD** spectra for ceramic glazes. *Below-* Profile of M. Fiske glaze prior to firing with vertical axis indicating peak intensity, horizontal axis in degrees 2θ. Spectra indicate quartz, anorthite, clinopyroxene, magnetite, hematite. *Above-* glaze after firing, spectra indicate quartz and amorphous glass.
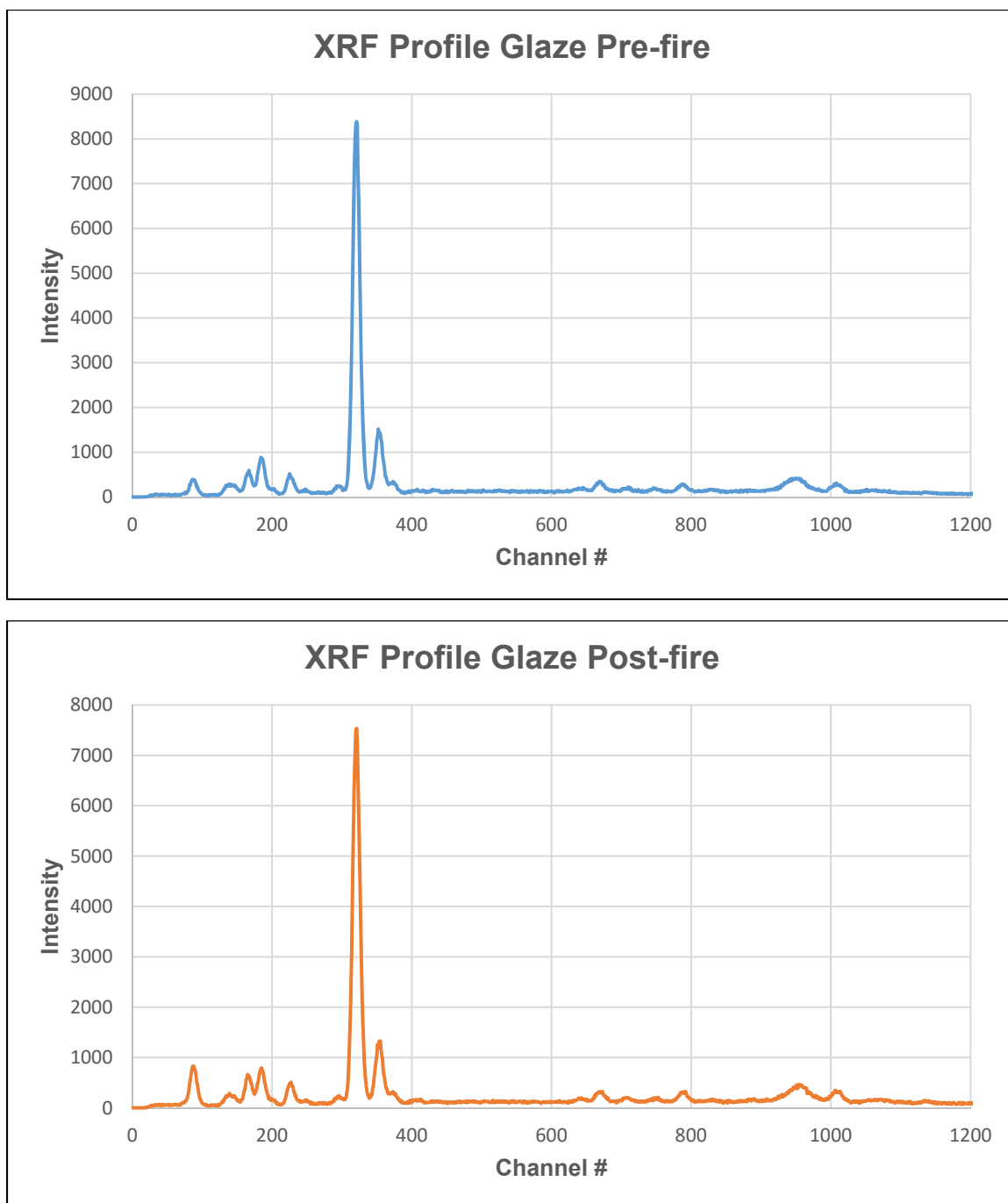
Figure 14. XRF analysis of glazes prior and post firing.   Characteristic diffraction peaks for Fe and Si.

Table 4. Rotary Shear Friction Experiments on Powdered Hematite

Experiment	1	2	3	4	5	6	7	8	9	10	11	12
Core Diameter (in)	0.71	1.00	1.00	1.00	1.00	1.00	1.00	1.00	1.00	1.00	1.00	1.00
Core Diameter (mm)	18.03	25.40	25.40	25.40	25.40	25.40	25.40	25.40	25.40	25.40	25.40	25.40
Contact Surface Area (in^2)	0.40	0.79	0.79	0.79	0.79	0.79	0.79	0.79	0.79	0.79	0.79	0.79
Gauge Measurement (psi)	500	500	1000	1500	2000	2000	2500	3000	3000	3500	4000	4500
Gauge Correction (lbs force)	885.00	885.00	1770.00	2655.00	3540.00	3540.00	4425.00	5310.00	5310.00	6195.00	7080.00	7965.00
Normal Stress (psi)	2235.37	1126.85	2253.70	3380.55	4507.40	4507.40	5634.25	6761.10	6761.10	7887.95	9014.80	10141.65
Normal Stress (Mpa)	15.41	7.77	15.54	23.31	31.08	31.08	38.85	46.62	46.62	54.39	62.15	69.92
Expected Torque (ft lbs)	10.47	14.75	29.50	44.25	59.00	59.00	73.75	88.50	88.50	103.25	118.00	132.75
Expected Torque (N m)	14.20	20.00	40.00	60.00	80.00	80.00	99.99	119.99	119.99	139.99	159.99	179.99
Max Torque Read (ft lbs)	7.90	6.20	11.10	38.50	28.50	42.20	51.80	50.30	44.80	72.10	87.90	106.40
Max Torque Read (N m)	10.71	8.41	15.05	52.20	38.64	57.22	70.23	68.20	60.74	97.75	119.18	144.26
% Difference Exp vs Max ft lbs	0.25	0.58	0.62	0.13	0.52	0.28	0.30	0.43	0.49	0.30	0.26	0.20
Coefficient Friction (µ)	0.45	0.25	0.23	0.52	0.29	0.43	0.42	0.34	0.30	0.42	0.45	0.48
Mean (µ)	0.38											
Standard Deviation (µ)	0.09											
Average Deviation (µ)	0.08											
Standard Error (µ)	0.03											

Table 4. Results of friction experiments.   Calculated and measured values from experiment results performed on powdered hematite using a rotary shear apparatus. Fields in yellow are input measurements and non-highlighted fields are calculated values of unit conversion or using *Equation 4.* Blue highlights the coefficient of friction. Note that only experiment 1 is performed using rock core, experiments 2-8 are performed using steel bar-stock.
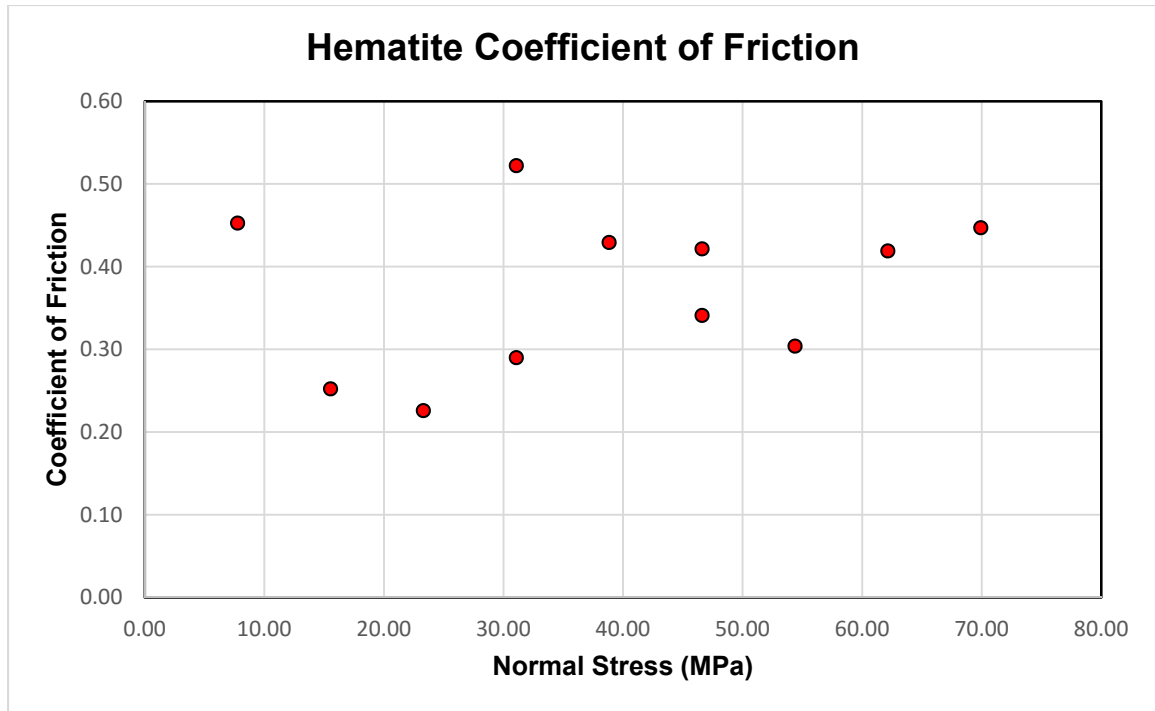
Figure 15. Coefficient of friction vs normal stress.
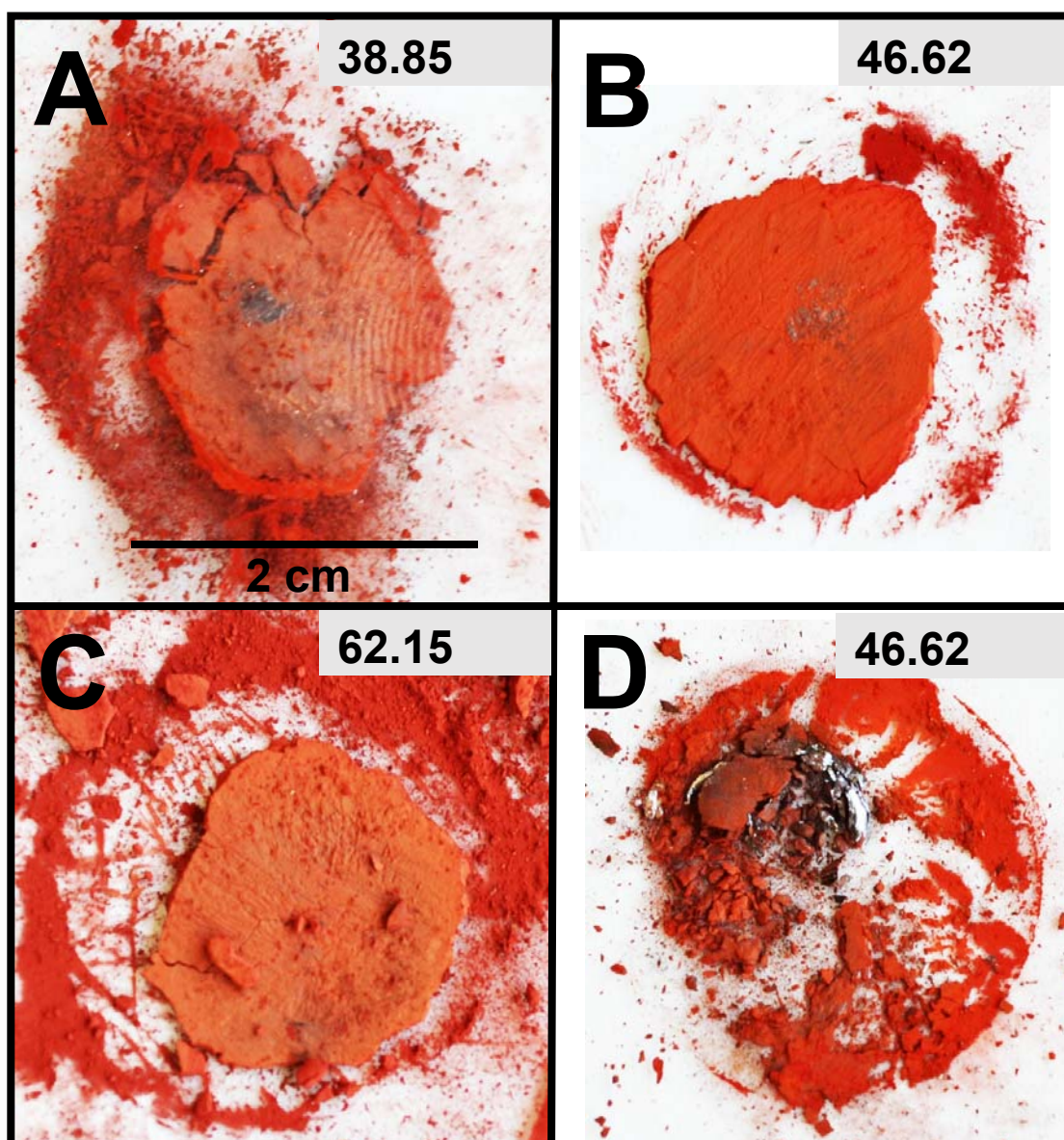
Figure 16. Photographs of synthetic hematite gouge. *A-C*, enhanced photographs of hematite from friction experiments, lifted from core, mounted on clear plastic tape. The lighter color hematite is the more deformed hematite compact. Halo around compacts shows extent of less consolidated deformed powder that does not adhere to tape. In A the lines are residual hematite in a fingerprint on the tape. *D* is the result of rotary shear of hematite gouge between to steel cores. Black material is residual from steel core, note the gradation in color in the rest of the hematite compact.

DISCUSSION

X-Ray Diffraction Resolution

In the tests to determine XRD standards, we found that small percentages (0% - ~15%) of magnetite relative to hematite are not discernable with X'Pert® XRD analysis. The X'Pert® XRD, therefore, has little utility in detecting small amounts of magnetite that can develop on fault surfaces in the rotary shear experiments or in natural samples. The low resolution of XRD analysis may be a product of non-homogeneity within samples and or require longer, constricted scan intervals over 30° and 49.5° 2θ. Either more reliable software or different instrumentation such as Mössbauer spectroscopy must utilized to establish a reliable standard as done in Betancur et al. (2003).

Composition of Ceramic Glazes

Ceramic glazes created by M. Fiske from basalt and rhyolite contain magnetite and hematite prior to firing (Fig. 13). Results of XRD after firing indicate that the basalt/rhyolite glaze is either an amorphous glass or microcrystalline. The lack of a reliable standard for magnetite/hematite percentages and the presence of both phases at the start of the experiment in unknown quantities make it difficult to determining whether neo-formed magnetite formed from hematite during firing. However, if the degree of crystallinity and proportion of magnetite versus other iron oxides could be established before and after firing, it could be determined whether neo-formed magnetite is present. SEM and BSE images taken before and after firing glazes could also help identify newly created magnetite. The XRF profiles indicate that the elemental composition of glaze is the same prior to and after firing. This is to be expected because, although reactions may occur, the glaze will maintain the same overall elemental composition.

Implications of Hematite Coefficient of Friction and Rotary Shear Experiments

Evans et al. (2014) used nominal values for normal stress, friction, slip velocity, rock thermal properties and estimated a temperature rise of 300 °C (Eqn. 1) along the small displacement faults in the footwall of the Wasatch Fault. A mean coefficient of friction value of 0.38 ±0.03 is much lower than the nominal 0.6 value used in the Evans et al. (2014) theoretical calculations of temperature rise, and is less than the μ found for westerly granite torsion experiments. With this lower coefficient of friction temperature rise due to frictional heating could be as low as 190°C, much lower than 300°C with all other variables held constant (Eqn. 1). A lower value of μ = 0.38 is more consistent with arguments made by Rempel and Rice (2006) who modeled thermal pressurization of faults using a coefficient of friction of 0.25. Rice (2006) calls on the effects of flash weakening of asperities to explain the diversion from the traditional 0.6-0.8 values predicted by Byerlee's Law.

The coefficient of friction varies with changes in the state of stress (Christensen et al., 1974). The fact that the rotary shear experiments presented are unconfined does raise the question of whether a μ = 0.38 is applicable to other states of stress, namely that of a fault that is under confining stress. The nature of rotary shear experiments under any amount of confining pressure still pose the problem of having a free surface at the edge of the comminuted material (Christensen et al., 1974). Measuring the maximum static coefficient of friction is unencumbered by the limitation of a free surface because by definition, no component of the experimental apparatus has moved including the hematite gouge. Under static conditions lateral forces acting to push hematite gouge out from the slip surface are in equilibrium with frictional forces keeping the hematite in between the cores.

Powdered hematite is used in place of the crystalline lithified hematite observed on small fault surfaces by Evans et al. (2014) and could result in a different coefficient of friction (Collettini et al., 2009). Powdered hematite is used because pure lithified hematite core would fail when subjected to high unconfined uniaxial stress just as the granodiorite core failed. Compacted materials with foliation or flow textured can have lower coefficients of friction than their powdered equivalents (Collettini et al., 2009).

A notable color change is observed in hematite compacts from friction experiments and rotary shear (Figs. 11, 15). There is distinct dark staining and contamination from the steel bar-stock meaning that at least some of the slip is accommodated between the bar-stock and powdered hematite. The coefficient of friction between the hematite power and bar-stock interface is likely lower and could potentially underreport the value of μ. SEM would be helpful in identifying potential changes in the morphology of the lighter colored hematite compact and comparing flow textures. Much of the hematite between the steel bar-stock is expelled during impact driven rotary shear. Further experimentation using hematite core and a more advanced rotary shear device must be performed. Such experiments would mitigate contamination and provide a mechanically homogeneous sample and a more reliable static coefficient of friction.

The detection of Fe^{2+} possible in the form of magnetite on the Wasatch fault indicates that temperatures exceeded 190 °C and at least passed through 450 – 470 °C (optimal non-equilibrium magnetite creation temperatures) during slip. Annealing textures identified by Ault et al. (2015) suggest even higher temperatures up to >750–800 °C. What then is the cause of additional heat generation? Adiabatic decompression suggested by O'Hara (2005) can produce a temperature rise or reduction of 336 – 879 °C in silicates.

These temperatures are derived from multiplying the Joule-Thompson coefficient by the compressive yield strength of the mineral. Quartz has a compressive yield strength of 2.8 GPa, however, hematite is only 0.1 – 0.4 GPa (Fan et al., 2012) assuming no preheating treatment or roasting prior to compression. If a Joule-Thompson coefficient for hematite is assumed to be similar to that of a silicate ~-300 °C/GPa (O'Hara, 2005), and multiplied by the compressive yield strength of hematite (0.1 – 0.4 GPa) then adiabatic temperature rise can be calculated to be 30-120 °C. If the upper estimates of both frictional and adiabatic heating are combined, the total temperature rise resulting from slip becomes ~310 °C, just shy of an optimal 450–470 °C for the formation of magnetite. Assuming a geothermal gradient of 30 °C/km, and supposing the hematite coated fault surfaces where at 5km depth at earthquake nucleation, the ambient temperature would be ~150 °C. Therefore, the total temperature of the Wasatch fault during seismic slip would be 460 °C.

Remaining Questions and Direction of Future Research

The annealing textures documented by Ault et al. (2015) and calculations by R. McDermott (Pers. Comm.) indicating high temperatures along the faults (~800 °C) that still require explanation. We expect that the flash temperature of 490 °C reported for the Wasatch fault is only the temperature of initial slip. As hematite is pre-heated or sintered its compressive yield strength increases (Wright, 1976; Fan et al., 2012). Flash heating from each subsequent slip event would strengthen hematite and increase flash heating temperatures relative to previous events. Future rotary shear experiments on hematite need to incorporate evolving compressive yield strength of hematite by pre-heating or sintering.

Run products from rotary shear with a controlled atmosphere and in the presense of moisture need to be performed. Ball-milling experiments have established that magnetite

can form from hematite due to active deformation of hematite powder and adiabatic decompression (Betancur et al., 2003). Future work will require the use of rotary shear in a controlled environment in order to investigate the morphology of hematite and magnetite post shear. This would establish a textural baseline with which fault related deformation in hematite within the slip zone can be compared. A more sophisticated rotary shear device would also enable the use of high confining stress so that representative rock core can be used in conjunction with a hematite gouge rather than steel bar-stock which contaminates samples.

CONCLUSIONS

Magnetite forms from hematite under specific pressure, temperature, and oxygen fugacity conditions and optimally when fO_2 is low, pressures are high, and temperatures are 350-570 °C for equilibrium conditions and 450-470 °C for non-equilibrium.

X-ray diffraction is not a reliable means for determining relative percentages of magnetite vs hematite. The coefficient of friction for powdered hematite synthetic fault gouge is 0.38 ±0.03. When this coefficient of friction is used in existing thermodynamic models, frictional temperature rise on the hematite coated surfaces are 190 °C. When geothermal gradient and adiabatic temperature rise are accounted for a flash heating temperature during seismic slip is ~460 °C, overlapping with the optimal conditions for magnetite formation summarized here. Color change in hematite compacts from friction experiments and rotary shear warrant further investigation into using more advance techniques such as SEM and more sophisticated machinery.

REFERENCES

Ashby, M.F., Abulawi, J., and Kong, H.S., 1991, Temperature Maps for Frictional Heating in Dry Sliding: Tribology Transactions, v. 34, p. 577–587, doi: 10.1080/10402009108982074.

Ault, A.K., Reiners, P.W., Evans, J.P., and Thomson, S.N., 2015, Linking hematite (U-Th)/He dating with the microtextural record of seismicity in the Wasatch fault damage zone, Utah, USA: Geology, p. G36897.1, doi: 10.1130/G36897.1.

Barrau, O., Boher, C., Gras, R., and Rezai-Aria, F., 2003, Analysis of the friction and wear behaviour of hot work tool steel for forging: Wear, v. 255, p. 1444–1454, doi: 10.1016/S0043-1648(03)00280-1.

Beeler, N.M., Tullis, T.E., and Goldsby, D.L., 2008, Constitutive relationships and physical basis of fault strength due to flash heating: Journal of Geophysical Research: Solid Earth, v. 113, doi: 10.1029/2007JB004988.

Betancur, J.D., Restrepo, J., Palacio, C.A., Morales, A.L., Mazo-Zuluaga, J., Fernández, J.J., Pérez, O., Valderruten, J.F., and Bohórquez, A., 2003, Thermally Driven and Ball-Milled Hematite to Magnetite Transformation: Hyperfine Interactions, v. 148-149, p. 163–175, doi: 10.1023/B:HYPE.0000003777.13951.7d.

Bhattacharya, A.K., and Arzt, E., 1992, Temperature rise during mechanical alloying: Scripta Metallurgica et Materialia, v. 27, p. 749–754, doi: 10.1016/0956-716X(92)90500-E.

Byerlee, J., 1978, Friction of rocks: Pure and Applied Geophysics, v. 116, p. 615–626, doi: 10.1007/BF00876528.

Campbell, S.J., Kaczmarek, W.A., and Wang, G.-M., 1995, Mechanochemical transformation of hematite to magnetite: Nanostructured Materials, v. 6, p. 735–738, doi: 10.1016/0965-9773(95)00163-8.

Christensen, R.J., Swanson, S.R., Brown, W.S., 1974, Torsional shear measurements of the frictional properties of westerly granite, NTIS, AD- 787 043.

Channer, M., and Ault, A., 2015, (U-Th)/He chronologic constraints on secondary Fe-oxide mineralization in southwestern New Mexico: Research Week, http://digitalcommons.usu.edu/researchweek/ResearchWeek2015/All2015/42.

Cole, D.R., Horita, J., Polyakov, V.B., Valley, J.W., Spicuzza, M.J., and Coffey, D.W., 2004, An experimental and theoretical determination of oxygen isotope fractionation in the system magnetite-H2O from 300 to 800°C 1: Geochimica et Cosmochimica Acta, v. 68, p. 3569–3585, doi: 10.1016/j.gca.2004.02.017.

Dejoie, C., Sciau, P., Li, W., Noé, L., Mehta, A., Chen, K., Luo, H., Kunz, M., Tamura, N., and Liu, Z., 2014, Learning from the past: Rare ε-Fe2O3 in the ancient black-glazed Jian (Tenmoku) wares: Scientific Reports, v. 4, doi: 10.1038/srep04941.

Di Toro, G., Han, R., Hirose, T., De Paola, N., Nielsen, S., Mizoguchi, K., Ferri, F., Cocco, M., and Shimamoto, T., 2011, Fault lubrication during earthquakes: Nature, v. 471, p. 494–498, doi: 10.1038/nature09838.

Essene, E.J., and Fisher, D.C., 1986, Lightning Strike Fusion: Extreme Reduction and Metal-Silicate Liquid Immiscibility: Science, New Series, Vol. 234, No. 4773 pp. 189-193

Evans, J.P., and Langrock, H., 1994, Structural analysis of the Brigham City-Weber segment boundary zone, Wasatch normal fault, Utah: Implications for fault growth and structure: pure and applied geophysics, v. 142, p. 663–685, doi: 10.1007/BF00876059.

Evans, J.P., Prante, M.R., Janecke, S.U., Ault, A.K., and Newell, D.L., 2014, Hot faults: Iridescent slip surfaces with metallic luster document high-temperature ancient seismicity in the Wasatch fault zone, Utah, USA: Geology, p. G35617.1, doi: 10.1130/G35617.1.

Fan, J., Qiu, G.Q., Jiang, T.J., Guo, Y.G., Hao, H.H., and Yang, Y.Y., 2012, Mechanism of high pressure roll grinding on compression strength of oxidized hematite pellets: Journal of Central South University, v. 19, p. 2611–2619, doi: 10.1007/s11771-012-1318-5.

Fondriest, M., Smith, S.A.F., Candela, T., Nielsen, S.B., Mair, K., and Toro, G.D., 2013, Mirror-like faults and power dissipation during earthquakes: Geology, v. 41, p. 1175–1178, doi: 10.1130/G34641.1.

Frost, B.R., 1991, Introduction to oxygen fugacity and its petrologic importance: Reviews in Mineralogy and Geochemistry, v. 25, p. 1–9.

Goldsby, D.L., and Tullis, T.E., 2011, Flash Heating Leads to Low Frictional Strength of Crustal Rocks at Earthquake Slip Rates: Science, v. 334, p. 216–218, doi: 10.1126/science.1207902.

Guo, Q., Shi, W., Liu, F., Arita, M., Ikoma, Y., Saito, K., Tanaka, T., and Nishio, M., 2013, Effects of oxygen gas pressure on properties of iron oxide films grown by pulsed laser deposition: Journal of Alloys and Compounds, v. 552, p. 1–5, doi: 10.1016/j.jallcom.2012.10.088.

M. Hashida, H. Mishima, S. Tokita, and S. Sakabe, 2009, Non-thermal ablation of expanded polytetrafluoroethylene with an intense femtosecond-pulse laser, Opt. Express **17**, 13116-13121

Lachenbruch, A.H., 1980, Frictional heating, fluid pressure, and the resistance to fault motion: Journal of Geophysical Research: Solid Earth, v. 85, p. 6097–6112, doi: 10.1029/JB085iB11p06097.

Lachenbruch, A.H., 1986, Simple models for the estimation and measurement of frictional heating by an earthquake: U.S. Geological Survey, 86-508, https://pubs.er.usgs.gov/publication/ofr86508 (accessed August 2015).

Li, W., Luo, H., Li, J., Li, J., and Guo, J., 2008, Studies on the microstructure of the black-glazed bowl sherds excavated from the Jian kiln site of ancient China: Ceramics International, v. 34, p. 1473–1480, doi: 10.1016/j.ceramint.2007.04.004.

Lindsley, D.H., 1991, Experimental studies of oxide minerals: Reviews in Mineralogy and Geochemistry, v. 25, p. 69–106.

Matthews, A., 1976, Magnetite formation by the reduction of hematite with iron under hydrothermal conditions: American Mineralogist, v. 61, p. 927–932.

McDermott, R., Ault, A., and Evans, J., 2015, Hematite (U-Th)/He dating as a tool for reconstructing million-year earthquake chronologies on the Wasatch Fault, Utah.: Research Week, http://digitalcommons.usu.edu/researchweek/ResearchWeek2015/All2015/283.

Moser, A.C., Evans, J.P., Ault, A.K., Janecke, S.U., Bradbury, K.K., Clausnitzer, S.M.,2015, Structural, geochemical, and thermal evolution of the southern San Andreas and parallel subsidiary faults in the Mecca Hills, southern California, AGU Fall Abst T41 A-2862

Noda, H., Kanagawa, K., Hirose, T., and Inoue, A., 2011, Frictional experiments of dolerite at intermediate slip rates with controlled temperature: Rate weakening or temperature weakening? Journal of Geophysical Research: Solid Earth, v. 116, p. B07306, doi: 10.1029/2010JB007945.

O'Hara, K., 2005, Evaluation of asperity-scale temperature effects during seismic slip: Journal of Structural Geology, v. 27, p. 1892–1898, doi: 10.1016/j.jsg.2005.04.013.

Otake, T., Wesolowski, D.J., Anovitz, L.M., Allard, L.F., and Ohmoto, H., 2010, Mechanisms of iron oxide transformations in hydrothermal systems: Geochimica et Cosmochimica Acta, v. 74, p. 6141–6156, doi: 10.1016/j.gca.2010.07.024.

Prante, M.R., Evans, J.P., Janecke, S.U., and Steely, A., 2014, Evidence for paleoseismic slip on a continental low-angle normal fault: Tectonic pseudotachylyte from the West Salton detachment fault, CA, USA: Earth and Planetary Science Letters, v. 387, p. 170–183, doi: 10.1016/j.epsl.2013.10.048.

Rempel, A.W., and Rice, J.R., 2006, Thermal pressurization and onset of melting in fault zones: Journal of Geophysical Research: Solid Earth, v. 111, p. B09314, doi: 10.1029/2006JB004314.

Rice, J.R., 2006, Heating and weakening of faults during earthquake slip: Journal of Geophysical Research: Solid Earth, v. 111, p. B05311, doi: 10.1029/2005JB004006.

Rice, J.r., 2015, Heating and weakening of faults during earthquake slip: So cal eq center annual mgt, plenary lecture, http://files.scec.org/s3fs-public/20150913_1800_Rice_Plenary.pdf

Sakthivel, R., Bhattacharyya, D., Eswaraiah, C., Das, D., Jayasankar, K., and Mishra, B.K., 2014, Effect of milling on reduction behavior of blue dust: Journal of Alloys and Compounds, v. 587, p. 677–680, doi: 10.1016/j.jallcom.2013.10.257.

Sanz, M., Oujja, M., Rebollar, E., Marco, J.F., de la Figuera, J., Monti, M., Bollero, A., Camarero, J., Pedrosa, F.J., García-Hernández, M., and Castillejo, M., 2013, Stoichiometric magnetite

grown by infrared nanosecond pulsed laser deposition: Applied Surface Science, v. 282, p. 642–651, doi: 10.1016/j.apsusc.2013.06.026.

Savage, H.M., Polissar, P.J., Sheppard, R., Rowe, C.D., and Brodsky, E.E., 2014, Biomarkers heat up during earthquakes: New evidence of seismic slip in the rock record: Geology, v. 42, p. 99–102, doi: 10.1130/G34901.1.

Schwarz, R.B., and Koch, C.C., 1986, Formation of amorphous alloys by the mechanical alloying of crystalline powders of pure metals and powders of intermetallics: Applied Physics Letters, v. 49, p. 146–148, doi: 10.1063/1.97206.

Shima, M., Tepper, T., and Ross, C.A., 2002, Magnetic properties of chromium oxide and iron oxide films produced by pulsed laser deposition: Journal of Applied Physics, v. 91, p. 7920–7922, doi: 10.1063/1.1451881.

Sibson, R.H., 1975, Generation of Pseudotachylyte by Ancient Seismic Faulting: Geophysical Journal of the Royal Astronomical Society, v. 43, p. 775–794, doi: 10.1111/j.1365-246X.1975.tb06195.x.

Siemes, H., Klingenberg, B., Rybacki, E., Naumann, M., Schäfer, W., Jansen, E., and Rosière, C.A., 2003, Texture, microstructure, and strength of hematite ores experimentally deformed in the temperature range 600–1100 °C and at strain rates between $10-4$ and $10-6$ s−1: Journal of Structural Geology, v. 25, p. 1371–1391, doi: 10.1016/S0191-8141(02)00184-0.

Solferino, G., and Anderson, A.J., 2012, Thermal reduction of molybdite and hematite in water and hydrogen peroxide-bearing solutions: Insights on redox conditions in Hydrothermal Diamond Anvil Cell (HDAC) experiments: Chemical Geology, v. 322–323, p. 215–222, doi: 10.1016/j.chemgeo.2012.07.006.

Spray, J.G., 1992, A physical basis for the frictional melting of some rock-forming minerals: Tectonophysics, v. 204, p. 205–221, doi: 10.1016/0040-1951(92)90308-S.

Suryanarayana, C., 2001, Mechanical alloying and milling: Progress in Materials Science, v. 46, p. 1–184, doi: 10.1016/S0079-6425(99)00010-9.

Takacs, L., 1998, Combustion Phenomena Induced by Ball Milling: Materials Science Forum, v. 269-272, p. 513–522, doi: 10.4028/www.scientific.net/MSF.269-272.513.

Takacs, L., 2002, Self-sustaining reactions induced by ball milling: Progress in Materials Science, v. 47, p. 355–414, doi: 10.1016/S0079-6425(01)00002-0.

Tepper, T., Ross, C.A., and Dionne, G.F., 2004, Microstructure and optical properties of pulsed-laser-deposited iron oxide films: Magnetics, IEEE Transactions on, v. 40, p. 1685–1690, doi: 10.1109/TMAG.2004.827215.

Tiwari, S., Choudhary, R.J., and Phase, D.M., 2009, Effect of growth temperature on the structural and transport properties of magnetite thin films prepared by pulse laser deposition on single crystal Si substrate: Thin Solid Films, v. 517, p. 3253–3256, doi: 10.1016/j.tsf.2008.11.074.

Toro, G.D., Niemeijer, A., Tripoli, A., Nielsen, S., Felice, F.D., Scarlato, P., Spada, G., Alessandroni, R., Romeo, G., Stefano, G.D., Smith, S., Spagnuolo, E., and Mariano, S., 2010, From field geology to earthquake simulation: a new state-of-the-art tool to investigate rock friction during the seismic cycle (SHIVA): RENDICONTI LINCEI, v. 21, p. 95–114, doi: 10.1007/s12210-010-0097-x.

Vallina, B., Rodriguez-Blanco, J.D., Brown, A.P., Benning, L.G., and Blanco, J.A., 2014, Enhanced magnetic coercivity of α-Fe2O3 obtained from carbonated 2-line ferrihydrite: Journal of Nanoparticle Research, v. 16, p. 1–13, doi: 10.1007/s11051-014-2322-5.

Wright, J.K., 1976, The effect of firing conditions on the Strength of Hematite compacts: Powder Technology, v. 14, p. 103–113, doi: 10.1016/0032-5910(76)80012-5.

Yetter, R.A., Risha, G.A., and Son, S.F., 2009, Metal particle combustion and nanotechnology: Proceedings of the Combustion Institute, v. 32, p. 1819–1838, doi: 10.1016/j.proci.2008.08.013.

CHAPTER 2

**Federal and Private Landownership's effect on Oil and Gas Drilling and Production
in the Southwestern Wyoming Checkerboard**

ABSTRACT

This study investigates oil and gas drilling and production outcomes on federal and private land using the randomized allocation of the Wyoming railroad land checkerboard. Geologic and production variables are held constant in the analysis of nearly 65,000 yearly production records and 4,000 oil and gas wells. Spatial and graphical analysis of drilling and production data indicate that BLM leases are developed systemically later than private leases, likely due to bureaucratic delay. Rigorous statistical analysis of the data presented is needed to establish correlations between regulations, commercial activity, and land use. This chapter of the report presents the primary data used in a collaborative effort between David Jenkins, Dr. Eric Edwards, and Dr. Trevor O'Grady, which work will use hypotheses derived from this report to generate quantitative results and conclusions.[1]

---

[1] Please note: the results and discussion are reported together as is typical in economics literature.

INTRODUCTION

Bureaucracy is often criticized for its inefficiency. Anecdotes of high levels of paperwork and long waits for decisions are common among people interacting with large bureaucratic organizations like the federal government. However, if these organizations provide different goods and services compared to less bureaucratic entities, efficiency evaluation can be difficult. Moreover, bureaucratic entities may work with goods and services that are valued differently than those with an expressed market value. Bureaucratic delay and caution may even be efficient in some cases (Prendergast, 2003). In addition, what consumers see as bureaucratic delay may be due to the complex nature of demands placed on the allocation and management of a resource or land parcel. For these reasons estimating the cost of bureaucracy, and channels through which these costs are manifest, are difficult. To examine the effect of bureaucratic processes on economic outcomes, this project examines how state, federal, and private land ownership affects oil and gas development and extraction. To address selection issues, the approach utilizes the randomized allocation of federal lands due to the Pacific Railroad Acts between 1862 and 1871, and state lands under the General Land Ordinance of 1785.

Federal ownership of large reserves of land in the western US has become an important and contentious policy issue. Although these lands have a myriad uses, the highest revenues are generated from the extraction of mineral resources, especially oil and natural gas, where they are available. There has been little positive empirical analysis of the effect of federal ownership on economic outcomes and efficiency. The Wyoming checkerboard, centered on the Union-Pacific Railroad line that formed the first transcontinental railroad, overlies valuable oil and gas fields in the Green River Formation and underlying Mesozoic

strata. These fields were undiscovered at the time the land was assigned and therefore offer a unique natural experiment to observe how differences in ownership affect outcomes. We are not aware of any studies examining oil and gas extraction using a natural experiment of land allocation. Akee (2009) examined a similar checkerboard allocation in an urban setting, finding land randomly allocated to an Indian tribe was valued less than that held privately. Although not utilizing random assignment, Fitzgerald (2010) examined land ownership regimes in federal lease auctions, finding that where mineral and surface rights are split, prices paid were lower.

The purpose of this project is to investigate differential outcomes of oil and gas drilling and production on federal and privately held land. This is accomplished by comparing nearly 65,000 yearly production records for almost 4,000 oil and gas wells located in the land checkerboard. Spatial and graphical interpretation of randomly assigned land ownership allows for all other explanatory variables related to geology and production to be held constant while revealing the effect of contracting and regulation. In other words, because the land has been randomly assigned, if drilling and production is not the same on private versus federal land, then that difference is likely due to aspects of differential regulation and/or contracting.

We hypothesize that: 1. fewer wells are drilled on federal land than private land because of high transaction costs related to regulation. 2. That production is higher on private land than federal.   3. Contract conditions will have an effect on a firm's choice to drill on private vs federal land.
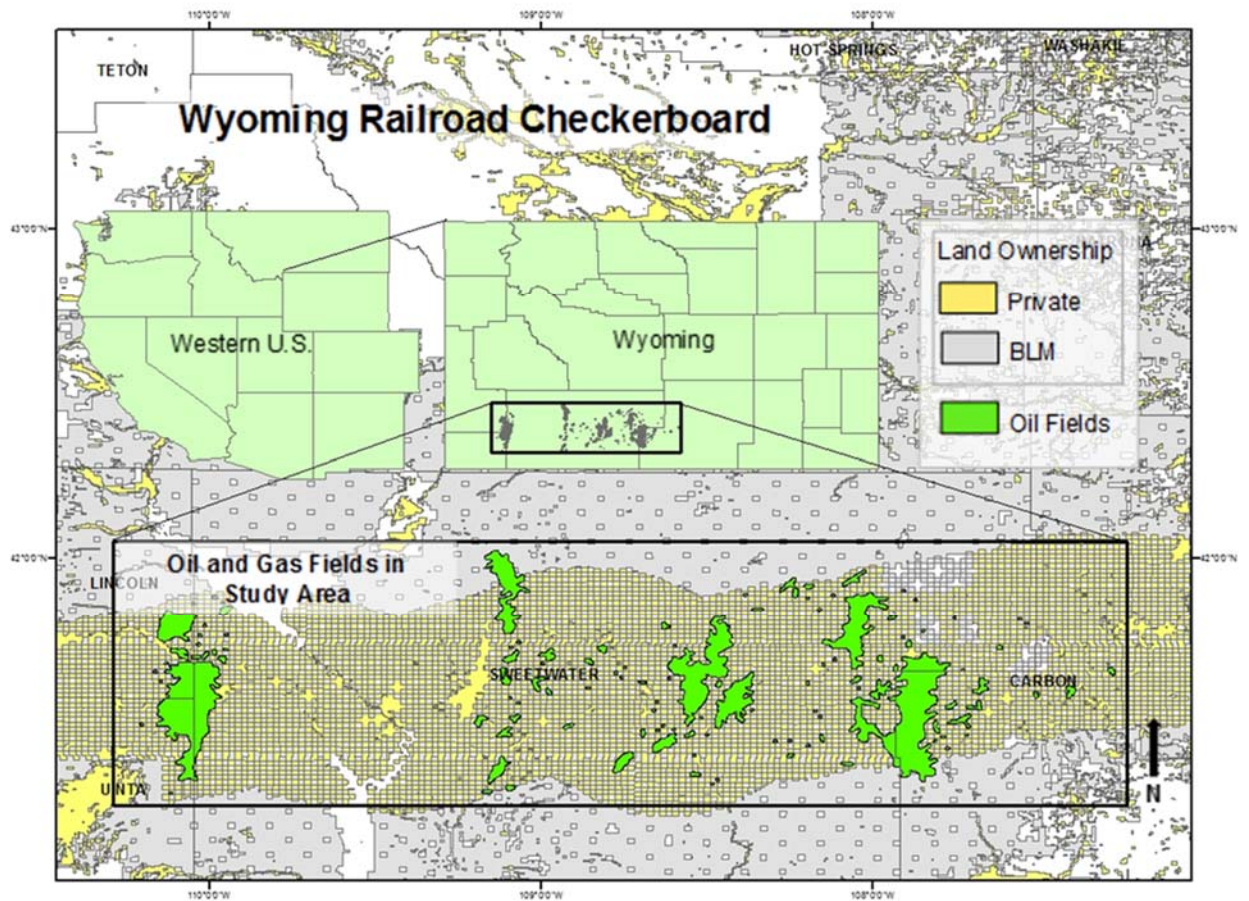
Figure 17. Wyoming Railroad Checkerboard. A generalized map of the study area and its associated oil and gas fields that lie within the checkerboard as well as land ownership.

BACKGROUND

Oil and Natural Gas Production

Oil and gas drilling and production typically occur in a heterogeneous geologic system where local geology determines well production. Once a well is drilled, a decline in production is expected over time (Arps, 1945). Production decline is influenced by reservoir characteristics such as porosity, permeability, how heavy hydrocarbons are relative to water (i.e. API gravity or specific gravity), and pore pressures of the reservoir. Therefore, analysis of decline curves can be used to infer reservoir characteristics (Archer and Wall, 1986a).

Hydrocarbons travel from regions of high to low pressure. When a well is drilled, an area of low pressure is created and is maintained by a mechanical pump (Archer and Wall, 1986). Because hydrocarbons are compressible, lighter hydrocarbons push heavier hydrocarbons and water to the wellbore in a mechanism called gas expansion drive (Fig. 17). Slightly different, but related, is dissolution gas drive where dissolved natural gas is liberated and pushes fluids to the wellbore. Initial production volumes are high when gas is the driving mechanism, but decline exponentially (Fig. 17). In water drive mechanisms, hydrocarbons are driven to the wellbore without the assistance of natural gas (Fig. 17). Water is thought to replace hydrocarbons in porespace, and replace them either partially or completely leading to a sustained high production yield for long periods of time (American Association of Petroleum Geologists, 2016).

The rate at which oil and gas is produced will influence how many wells an oil company will drill and where to drill them. A rule of thumb is that gas drive reservoirs have more wells drilled with smaller spacing because production declines quickly and the reservoirs are compartmentalized. In contrast, water drive reservoirs have fewer wells with

larger spacing because high initial production is sustained and oil moves more freely between wells. In either case, when drilling occurs is almost as important as where it occurs, because the first wells to produce will yield the highest production due to high initial reservoir pressures (Archer and Wall, 1986). In a water drive reservoir timing is especially important because initial production has a combined gas/water drive effect, and pressure for the entire reservoir can decrease as the number of wells increases (Archer and Wall, 1986).

Eventually, oil field production will decrease to the point where wells are no longer economic to operate because the costs of maintenance costs far outweigh production gains. Oil companies can then choose to either plug and abandon wells, re-stimulate wells via hydraulic fracturing on other potential producing horizons, inject fluids (water or CO_2) into the reservoir pushing residual oil and gas to producing wells (Archer and Wall, 1986), or abandon them entirely after a "blow-down" in which a controlled depressurization of the wellbore is conducted.

Contracting

Commonly landowners do not drill their own wells. In these cases, federal, state, or private land can go for lease auction in which the landowner receives a small upfront payment in exchange for providing an oil company the option to drill on their land for a specified period of time. If oil is produced by a well on the property, the landowner receives a royalty payment, which is percentage of the gross value of oil extracted. There are significant differences in contract structure between federal and private leases, in large part because federal lease structure is standardized and private leases are not. Private lease duration is typically 3-5 years, while nearly all federal leases in Wyoming have a duration of 10 years. On BLM land, royalties paid to the Federal Government are 12.5% (Snow, 2015)

where royalties on private land range up to 25% (Riley Brinkerhoff, pers. comm., 2015). Both BLM and private leases can only be held under continuous economic production.

Wyoming BLM parcels are auctioned quarterly using a competitive sealed-bid first-price auction. Unsold leases are available to be purchased non-competitively. Remaining parcels without a buyer are then recycled through the auction. The price of a typical BLM lease with a 10 year term ranged from $17-$223 per acre from 1998-2013 (Bureau of Land Management, 2016). Private parcels can be marketed individually to potential buyers or sold in open auction. Because these sales are private, it is difficult to obtain sales records that include per acre prices. However, industry sources indicate private parcels in Wyoming vary in duration and sell for roughly $300 per acre, depending on the resource quality (M. Dighans, pers. comm., 2016).

The amount of time required for a drilling permit to be granted on BLM land can be much longer than on private land (M. Dighans, pers. comm., 2016). The BLM permitting process to drill or recomplete a well can take anywhere from nine months to two years depending on stipulations attached to the permit. Delays are often due to the time required to assess and comply with the National Environmental Policy Act (NEPA) of 1970, Federal Land Policy Management Act (FLPMA) of 1976, Endangered Species Act (ESA) of 1973, and National Historic Preservation Act (NHPA) 1966. Evaluation and compliance with these enacted laws is performed by third party consulting firms prior to receiving a permit to drill, recomplete, or inject in wells and can cost tens of thousands of dollars ("Leasing," 2016; B. Burger, pers. comm., 2016).

The Railroad Checkerboard

The Pacific Railroad Acts of 1862 and 1871 granted every other section (1 mi^2) of land within twenty miles of either side of the railroad (U.S. National Archives, 2016)(Fig. 17). When Wyoming became a state, every sixteenth section was granted to the State and many of those sections were set aside as school trust lands (Office of State Lands and Investments, 2016). What remains is a geometric patchwork of Bureau of Land Management (BLM) and privately held land crossing southern Wyoming. This unique allocation of land provides an ideal natural experiment for examining oil and gas production by land ownership.

The federal and private land types are equally likely to have the same reservoir characteristics, geology, and production drive mechanisms because land is randomly allocated and the area of most of the oil and gas pools are $> 1mi^2$ (DeBruin, 1989). However, because production decreases over time, if wells are drilled systemically later on a particular land type, then it is expected that the land drilled later will have lower production. Other variation in producing behavior on federal vs private land is due to oil companies choosing to drill on whatever land type best maximizes profit, or to "prove up" a geologic or engineering concept on private or state lands before going through the federal land permitting process. No other studies have made use of the railroad checkerboard to investigate outcomes of oil and gas drilling. One paper appearing in the *American Economic Review* made the attempt, however was redacted because of mistakes in well production data (E. Edwards, pers. comm., 2015).
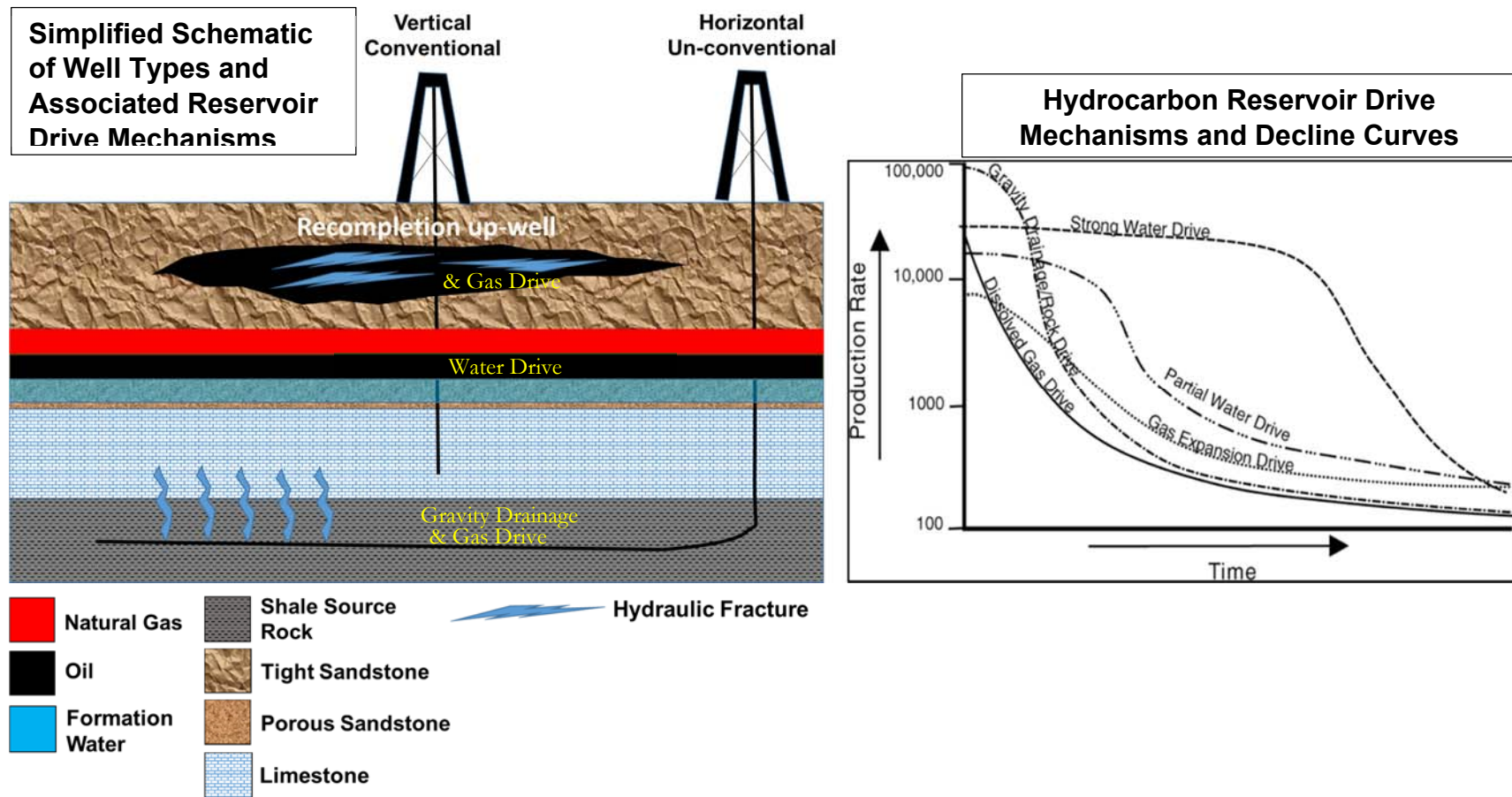
Figure 18. Reservoir drive mechanisms. Difference between conventional and unconventional wells and the associated decline curves with reservoir drive mechanisms (decline curves from ("Reservoir drive mechanisms - AAPG Wiki")). Horizontal drilling is not discussed in the text because to our knowledge, none exist in the study area. Drive mechanisms for horizontal wells are presented in this figure as a point of reference for future studies that may address them.

METHODS

To analyze the effect of land ownership on oil and gas production in the Wyoming checkerboard, 193,715 yearly oil and gas well production records were obtained from the Wyoming Oil and Gas Commission. In addition, shapefiles that delineate land ownership by section and outlines of oil and gas fields were retrieved from the BLM (Bureau of Land Management, 2012) and the State of Wyoming (Wyoming Oil and Gas Conservation Commission, 2016). Two complete datasets are collected from the Wyoming Oil and Gas Commission. The first is oil and gas cumulative production data for each well from initial production in the early 1900's until 2010. Most of the development in the study area began in the 1950's, so this dataset will be hereafter referred to as the 1950 dataset. The second dataset is a high frequency dataset that records monthly production from 1978 to 2015. The 1978 dataset will be used for more rigorous econometric analysis to test hypotheses derived from the 1950 dataset. The datasets overlap from 1978 to 2010 and differ slightly from each other for this period of time.

Although individual well data is available, production is aggregated by section: all of the wells on a particular section will have production added together. Production is often misallocated for any particular well because measurements are taken at the collection tanks rather than at the well head. Well production data also comingle the production from all of the producing horizons in the well. Section-level production volumes are a more accurate metric and correspond with the unit of land ownership.

GIS analysis of oil and gas records is used to ensure the random distribution of land ownership and geologic control. Oil and gas field shapefiles are chosen that completely sit within the checkerboard landownerships. Fields are then reduced to those that sit within the

geologic Green River Basin extents as indicated by an overarching shapefile. Viewing fields within a single hydrocarbon producing basin is important, because natural heterogeneity is reduced from well to well, oil can be assumed to maintain a similar specific gravity, be produced from similar formations and depths, and sourced from similar formations. Geologic control is significant in selecting fields to compare because the less variability there is in the subsurface, the more variability can be attributed to drilling and producing behavior of landowners. Only oil and gas wells within the bounds of the selected oil fields were chosen for comparison. By doing so, complicated land ownership types attributed to multiple government agency jurisdictions and out-of-basin wildcat drilling behavior is removed. Production and drilling data are compared with shapefiles to remove sections with split ownership types, non-random distribution of land within a field, or wells attributed to ownership by both the BLM and private land because of shared borders or incorrect GIS datum conflicts. After cleaning, 64,777 yearly production records remain.

The production and drilling data are plotted in several ways to highlight differences in outcomes on BLM and private land. In the 1950 dataset, values are reported based on start date, stop date, and sum total production of oil and natural gas, referred to as *ultimate recovery*.

The plots used to display this data are: ultimate recovery vs time, cumulative ultimate recovery vs time, number of wells drilled vs time, cumulative wells drilled vs time, and ultimate recovery vs wells drilled in any given year. The ultimate recovery vs time plot illustrates how successful wells are that start production in any given year. Cumulative ultimate recovery is a running total of ultimate recovery through time that reveals potential disparities in total production between land types. Number of wells drilled is the total

number of wells drilled in a given year. The cumulative number of wells drilled is an additive measure of number of wells drilled. Drilling activity plots can indicate oil companies reactions to commodity prices, regulation, and/or contract changes. A measure of relative efficiency is determined when the number of wells drilled is plotted against ultimate recovery.

Commodity prices are important in the interpretation of drilling and production behavior through time. The prices plotted are inflation adjusted using the Consumer Price Index (CPI) so that prices can be compared through time (Fig. 20a-b). The historic Illinois Crude oil price is plotted in tandem with the Henry Hub natural gas price (Fig. 21).

Plots derived from the 1950 dataset and selected plots from the 1978 dataset are displayed generally for the entire study area. Granular analysis of the data is not recommended at this point. Instead, a generalized view of the data is used to develop hypotheses regarding events that may have impacted land-lease selection over the past forty years. Forthcoming econometric analysis will quantitatively test the hypotheses postulated in this report.

**Oil Fields: Oil Favorability, Land Ownership, and Well Placement**
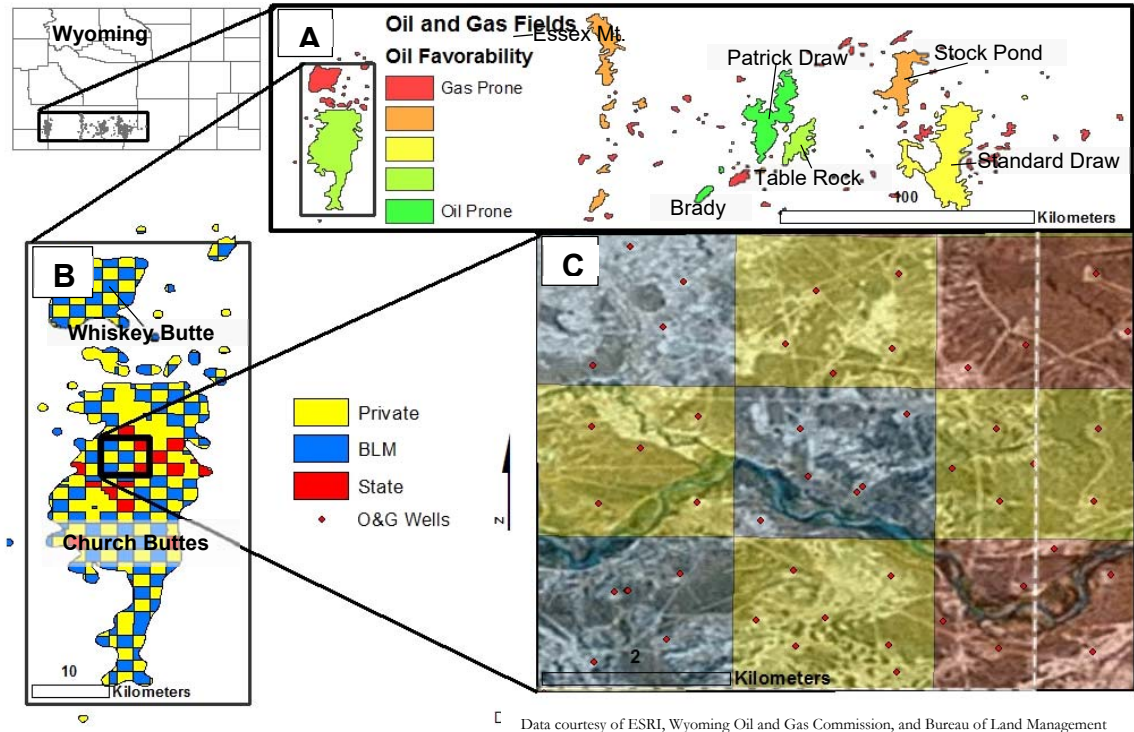
Figure 19. Oil fields and ownership. **A**- Oil and gas fields whithin the study area ranked by quantities of oil produced, larger fields have names displayed. A total of 118 individual fields lie within the study area. **B**- An expanded view of Church Buttes field with the associated land ownership. **C**- An orthographic image of Church Buttes field with BLM, private, and State lands highlighted with their corresponding color code. Red points are the surface locations of oil and gas wells. Colored squares are 75% transparent revealing surface topography.
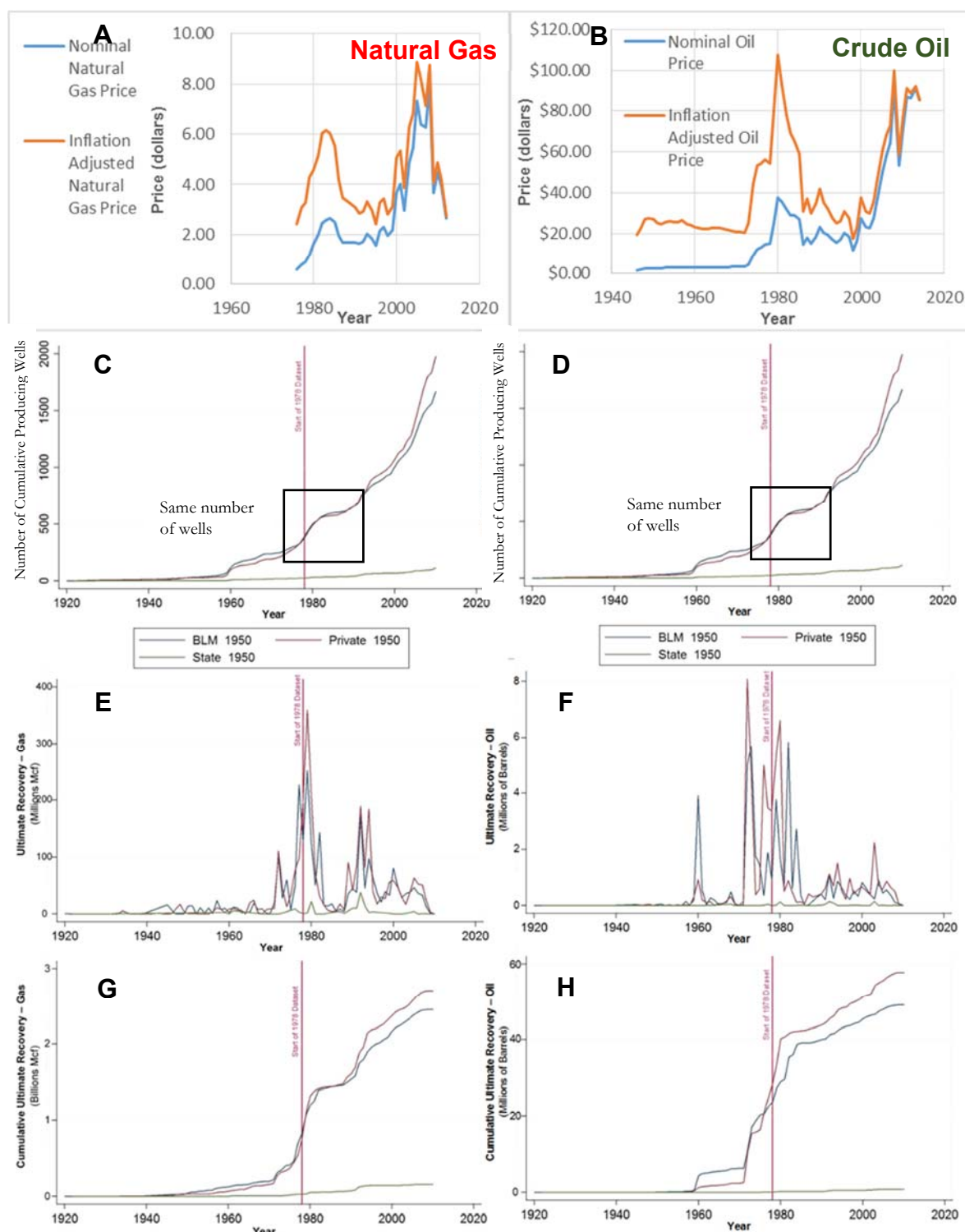
*Larger versions of plots in appendix

Figure 20. A-H. Comparison plot of production and prices. Wells drilled, production, and cumulative production from the 1950 dataset. *Gas-left, Oil-right.* Ultimate Recovery is the sum total of production of wells assigned to the year wells were drilled. Cumulative Ultimate Recovery is a running total of Ultimate Recovery.
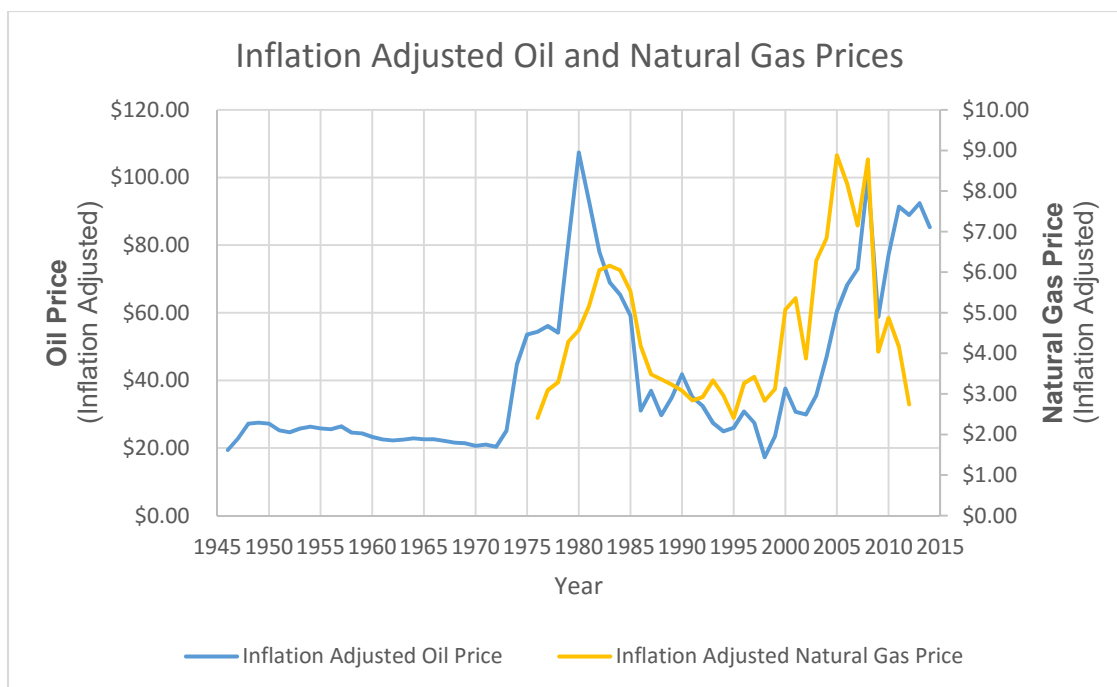
Figure 21. Inflation adjusted oil and natural gas prices.
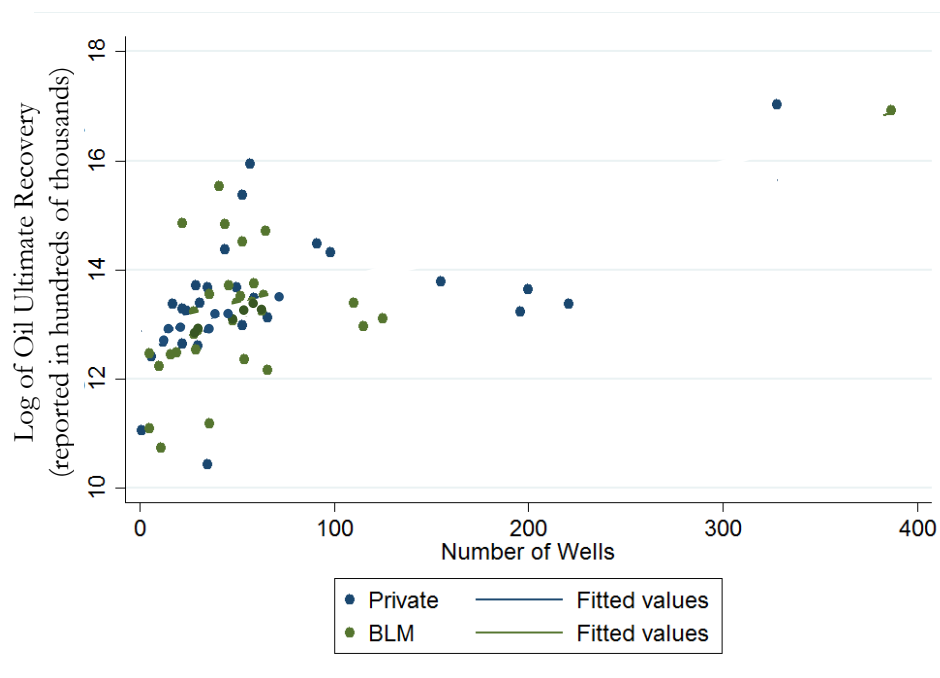
Figure 22. Ultimate recovery of oil vs number of wells drilled. Each point represents a year and that years associated ultimate recovery and number of wells drilled.
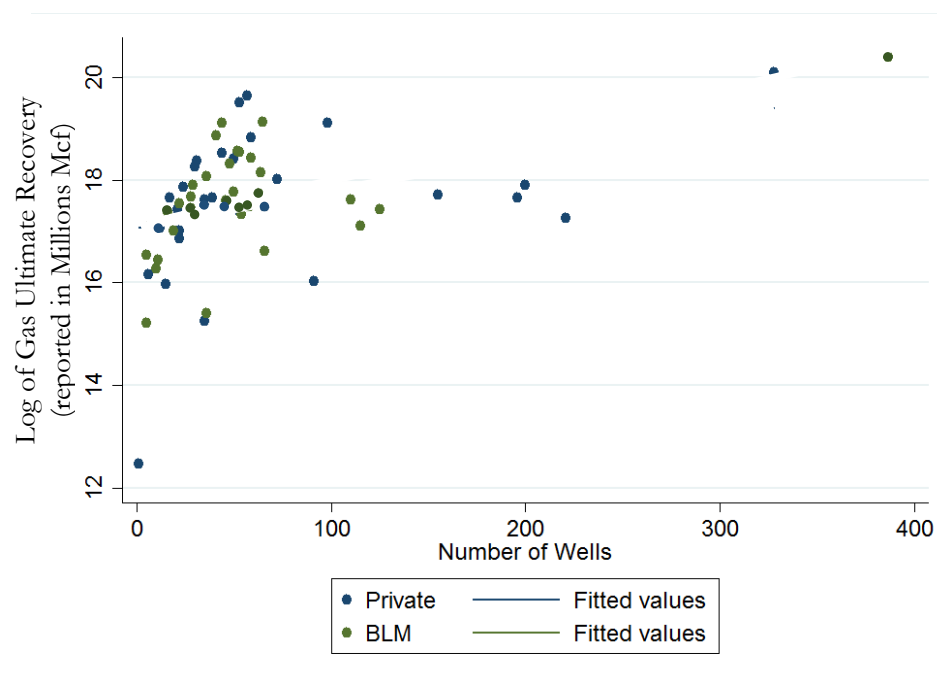
Figure 23. Ultimate recovery of gas vs number of wells drilled. Each point represents a year and that years associated ultimate recovery and number of wells drilled.

RESULTS AND INITIAL FINDINGS

We hypothesize that: (1) fewer wells are drilled on federal land than private land because of high transaction costs related to regulation and (2) production is higher on private land than federal land. (3) Also, we expect that contract conditions will have an effect on a firm's choice to drill on private or federal land. Results from analysis of drilling and production data that are used to test these hypotheses are discussed below.

Oil and Natural Gas Prices

Oil companies cannot predict when the highest price will occur, however, they will respond to a price increase relative to the previous period. Thus, we would expect that the highest volumes of drilling production occur during increasing prices. Likewise, we would expect drilling and production to fall or remain constant during decreasing prices This general response to prices is evident in drilling behavior within the checkerboard (Fig. 20 a,b). The effect of price change should influence drilling behavior in the same fashion on all land types if all other variables are held constant.

The same or similar numbers of wells are drilled on BLM and private leases under a range commodity prices (Figs. 20a-d), which partially refutes the notion that drilling behavior is different between land types. As an exception, after year(s) ~1994 cumulative numbers of producing wells diverge with an increase in private drilling. Interestingly, this divergence occurs while prices are decreasing, meaning oil companies may be reacting to incentives other than price and preferentially drilling on private leases. To investigate the cause of the divergence in drilling behavior in 1994 rigorous statistical treatment of the data will need to be employed. Hereafter, analysis is limited to points in time when wells drilled on both land types are the same, because graphical comparison of production is more direct and suitable

for interpretation. Since the numbers of wells drilled are similar, we would expect production to be similar on both land types because landownership is randomly assigned and each lease type stands equal probability of high resource quality.

Ultimate Recovery and Cumulative Ultimate Recovery of Oil and Gas

Cumulative oil production is higher on private land than federal land prior to 1994, but not necessarily for natural gas (Fig. 20 e-h). Reservoir drive mechanisms are likely responsible for the production disparity. Spikes in ultimate recovery of oil and natural gas on BLM land lag 1-2 years behind private (Fig. 20 e-f). Meaning the 1-2 yr well permitting process on BLM land leads oil and gas firms to preferentially develop private land first. Private wells drilled first exploit initial high water drive reservoir pressures leaving diminished production for BLM wells drilled later (Fig. 18). Since gas drive reservoirs in the checkerboard are not well connected, cumulative gas production for any given well is expected to be the same regardless of when a well is drilled.

Private leases react to rising prices quickly, causing production to be uniform as prices increase. The extensive permitting process on BLM land instigates delayed reactions to price changes leading to punctuated development. Although BLM and private leases have the same cumulative ultimate recovery of gas before 1994, revenues between land types vary because BLM gas volumes are sold for lower prices (Figs. 20a, g). This may indicate an efficiency gap and can only be solved through detailed cost benefit analysis.

Private cumulative ultimate recovery of natural gas is greater than BLM from 1994 until 2010 (Fig. 20g). This could simply be a reflection of more wells being drilled on private leases. Periods of increased drilling correspond with greater ultimate recovery volumes for natural gas, but not always for oil (Figs. 20e-f, 22, 23). This is because very few fields in the

checkerboard are favorable for oil production and their reserves are depleted prior to 1994 (Fig. 19). Patrick Draw, Brady, and Table Rock are oil fields with water drive reservoirs (Fig. 18), and produce a majority of the oil in the checkerboard (Street, 1979).

Contract structure differences between federal and private leases to not appear to impact a firm's decision to choose BLM or private land, because more expensive private leases are being chosen for first development. What seems to be a more important factor is the amount of time permits take to be granted. In other words, because of reservoir drive mechanisms, when you drill is as important as where you drill.

Relative Efficiency

Cross-plots of the number of wells on BLM and private lands as a function of ultimate recovery reveal similar correlations for both oil and gas production (Figs. 22-23). Until multivariate statistical analysis is performed, the relationships between the number of oil and gas wells and production remain inconclusive.

Potential Causes and Future Research

In order to drill quickly, the lengthy time required for permitting causes oil companies to drill on private rather than federal land. The Energy Policy Act of 1992 and sale of the Union Pacific Resource Group in 1995 (15% stake sold in an Initial Public Offering (IPO)) and 1996 (87% stake sold in an IPO) are both candidates for changes in lease selection and oilfield development post 1994 (Strack, 2015). The federal government sought to incentivize clean energy with the Energy Policy Act of 1992 and may have caused restructuring in federal mineral leasing policy, and therefore dis-incentivized drilling for hydrocarbons on BLM land. Separately, but in a similar time-period, the Union Pacific

Resource Group may have increased production in the early nineties in order to maximize revenue from their IPO.

We also propose that environmental protection of the greater sage grouse habitat, and pre-existing policies which cause bureaucratic delay are reasons for the widening gap in producing wells post year 2000 (Kirol et al., 2015) In 2003, the cumulative producing well disparity between private and BLM drilling widens at an increasing rate (Figs. 20c-d). Incentives for oil field development in 2003 are relatively high commodity prices, and opportunities for water/CO_2 flood projects for additional oil recovery (Lim and Ramsey, 2006).

A difference in difference econometric model will be used for further testing the treatment effect of regulatory policy, corporate activity, and contract structure on oil and gas drilling and production outcomes. This type of model assumes all variables, excluding those that are being tested, are held constant and reveals the impact of regulatory policy, corporate activity, and contract structure. The randomized allocation of land allows for the assumptions of a difference in difference model to be met. The 1978 high frequency panel dataset provides the necessary resolution to make granular observations and establishes a correlation in a quantitative manner. Analysis will then be taken to the field level rather than the breadth of the study area. A field level analysis will reveal the true effect of reservoir drive mechanisms on production and help establish whether federal leases are actually being developed later.

If our model of reservoir drive mechanisms is correct, and BLM wells are being drilled later, then they should have higher cumulative water production than private wells. The 1978 dataset contains observations of water production that will be used as a proxy for

costs and for decline curve analysis. This dataset will show the effects of water and CO_2 flooding of fields and serves to inform how oil companies are making secondary recovery decisions.

Oil companies often recomplete wells rather than plugging and abandoning them and may treat exhausted wells differently depending on the land type. The current analysis using ultimate recovery does not reveal the effects of recompletion, because the 1950 dataset only reports sum totals of production and is blind to changes in production over time. The 1978 dataset, however, will reveal whether a recompletion ever occurred and which land types are likely to have recompleted wells. Recompletions will display as a spike in production for a well that would otherwise be declining. In addition to revealing recompletion activity, monthly production data that is amenable to decline curve analysis will be used to determine reservoir drive mechanisms.

CONCLUSIONS

Oil and gas drilling and production outcomes for BLM and private leases are visible due to a randomized treatment of land ownership. Drilling behavior on BLM and private leases wax and wane according to price and a similar number of wells appear to be drilled on BLM and private land prior to 1994. Bureaucratic delay may be causing BLM leases to be developed in low price environments and with lower oil production. Oil wells drilled later on BLM land often produce less because of depleted reservoir pressures from earlier production on private land. Contract structures do not appear to impact whether an oil company will choose to drill on private versus federal land. Rigorous statistical treatment is still needed to test hypotheses and to establish correlations between regulation and contracting to oil and gas drilling outcomes.

REFERENCES

Archer, J.S., and Wall, C.G., 1986, Characteristics of Reservoir Rocks, *in* Petroleum Engineering, Springer Netherlands, p. 62–91, http://link.springer.com/chapter/10.1007/978-94-010-9601-0_5 (accessed March 2016).

Archer, J.S., and Wall, C.G., 1986, Secondary Recovery and Pressure Maintenance, *in* Petroleum Engineering, Springer Netherlands, p. 173–190, http://link.springer.com/chapter/10.1007/978-94-010-9601-0_11 (accessed March 2016).

Arps, J.J., 1945, Analysis of Decline Curves: Transactions of the AIME, v. 160, p. 228–247, doi: 10.2118/945228-G.

Oil and Gas Journal, 2016, no aurthor, BLM proposes higher onshore oil, gas royalty rates, http://www.ogj.com/articles/2015/04/blm-proposes-higher-onshore-oil-gas-royalty-rates.html (accessed March 2016).

DeBruin, R.H, 1989, Wyomings's Oil and Gas Industry in the 1980's a Time of Change, WGS: Public Information Cicular, No. 28

U.S. Bureau of Land Management, 2012, http://www.blm.gov/wo/st/en/prog/energy/geothermal/geothermal_nationwide/Documents/GIS_Data.html (accessed March 2016).

Kirol, C.P., Sutphin, A.L., Bond, L., Fuller, M.R., and Maechtle, T.L., 2015, Mitigation effectiveness for improving nesting success of greater sage-grouse influenced by energy development: Wildlife Biology, v. 21, p. 98–109, doi: 10.2981/wlb.00002.

BLM, 2016, http://www.blm.gov/wy/st/en/programs/energy/Oil_and_Gas/Leasing.html (accessed April 2016).

Lim, F.H., Ramsey, H.N., 2006, The Monell unit of the Patrick Draw field, Wyoming: CO2 flood in an old field using new technology: AAPG Search and Dis. Art. #90055.

Office of State Lands and Investments, http://lands.wyo.gov/ (accessed March 2016).

U.S. National Archives, Our Documents, *100 Milestone Documents from the National Archives*

- Pacific Railway Act (1862), http://www.ourdocuments.gov/doc.php?flash=true&doc=32 (accessed March 2016).

American Association of Petroleum Geologists - AAPG Wiki, http://wiki.aapg.org/Reservoir_drive_mechanisms (accessed March 2016).

Strack, D. Union Pacific Corp. Subsidiaries: UtahRails.net, http://utahrails.net/up/up-corp-subsidiaries.php (accessed April 2016).

Street, B.A., 1979, Patrick Draw (Monell Unit): Wyoming Oil and Gas Fields Symposium, Greater Green River Basin, p. 276–276.

Wyoming Oil and Gas Conservation Commission, http://wogcc.state.wy.us/ (accessed March 2016).

APPENDIX
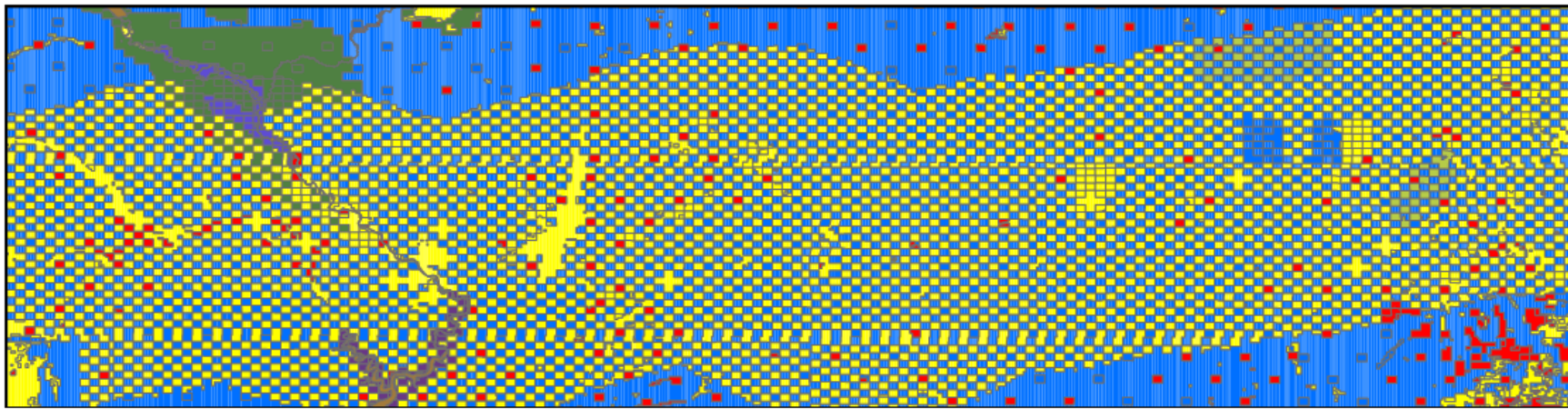
Land Ownership

☐ all other values

SURFACE

☐ Bureau of Indian Affairs	☐ Forest Service
☐ Bureau of Land Management	☐ Local Government
☐ Bureau of Reclamation	☐ National Grasslands
☐ Corps of Engineers	☐ National Park Service
☐ Department of Agriculture	☐ Private
☐ Department of Defense	☐ State Trust
☐ Department of Energy	☐ State (State Parks & Hist Sites)
☐ Department of Veterans Affairs	☐ State (Wyoming Game & Fish)
☐ Fish & Wildlife Service	☐ Water

Figure 24 Land ownership for Southwestern Wyoming. Surface rights and mineral rights are largely owned by the same entity
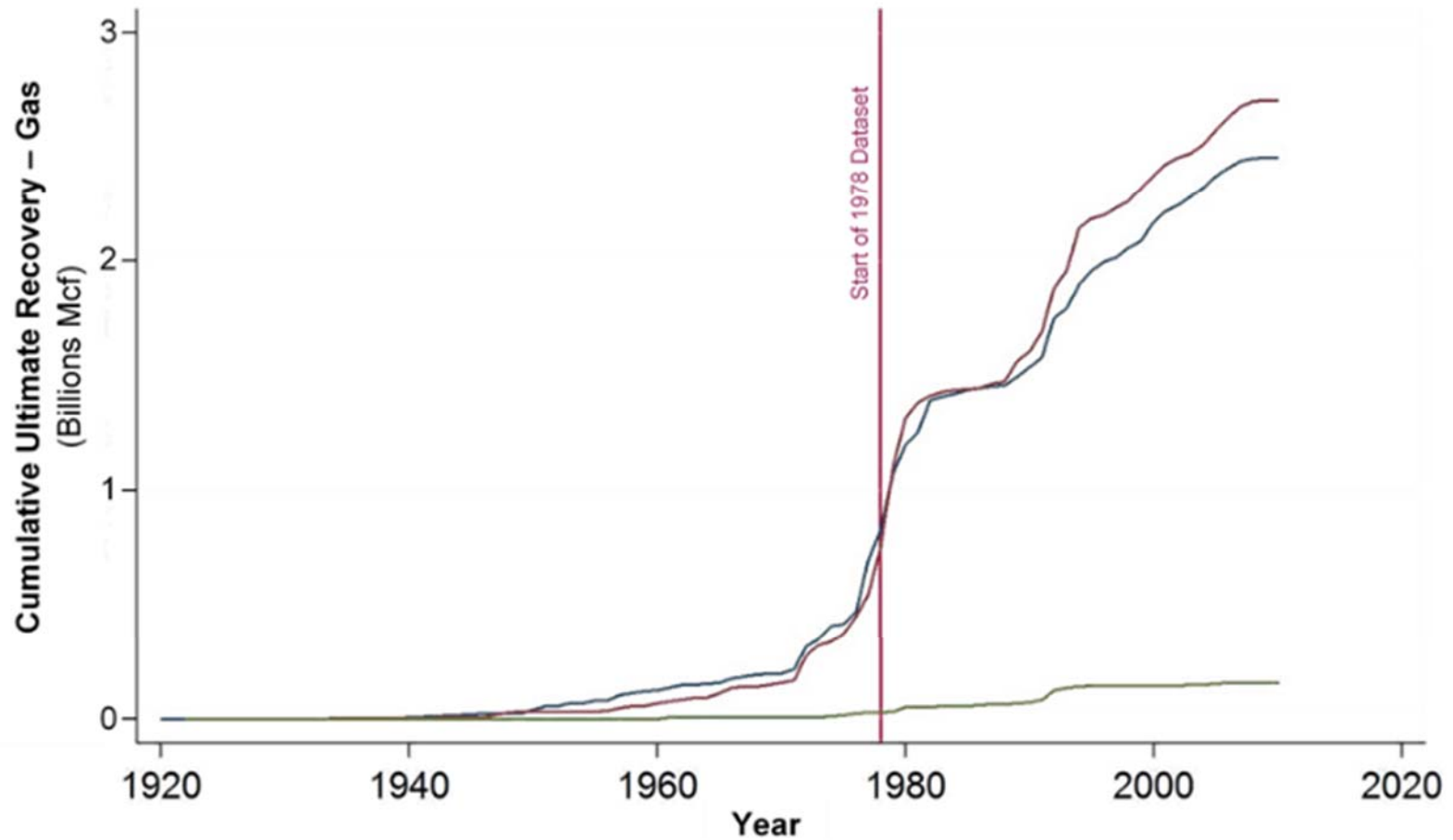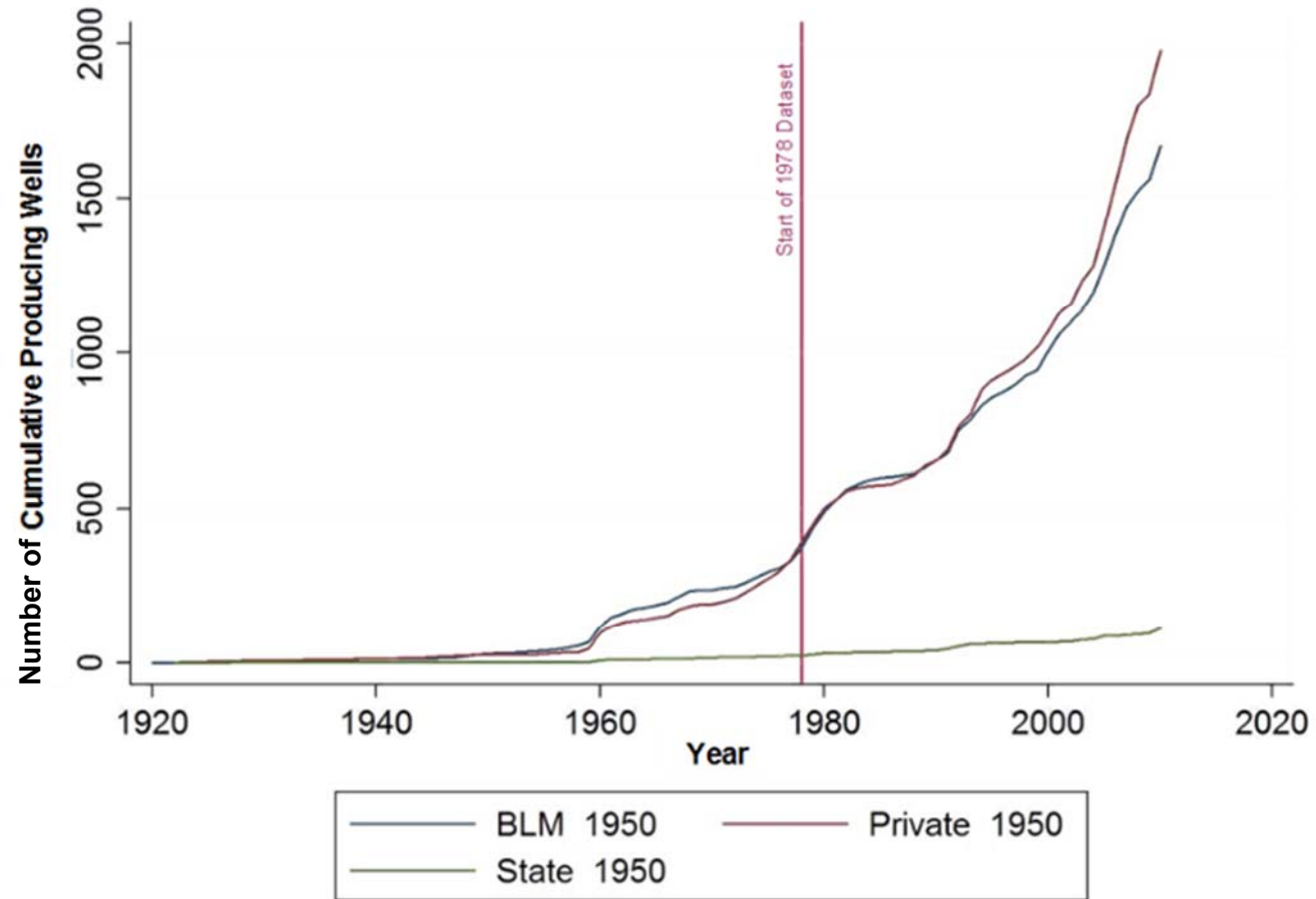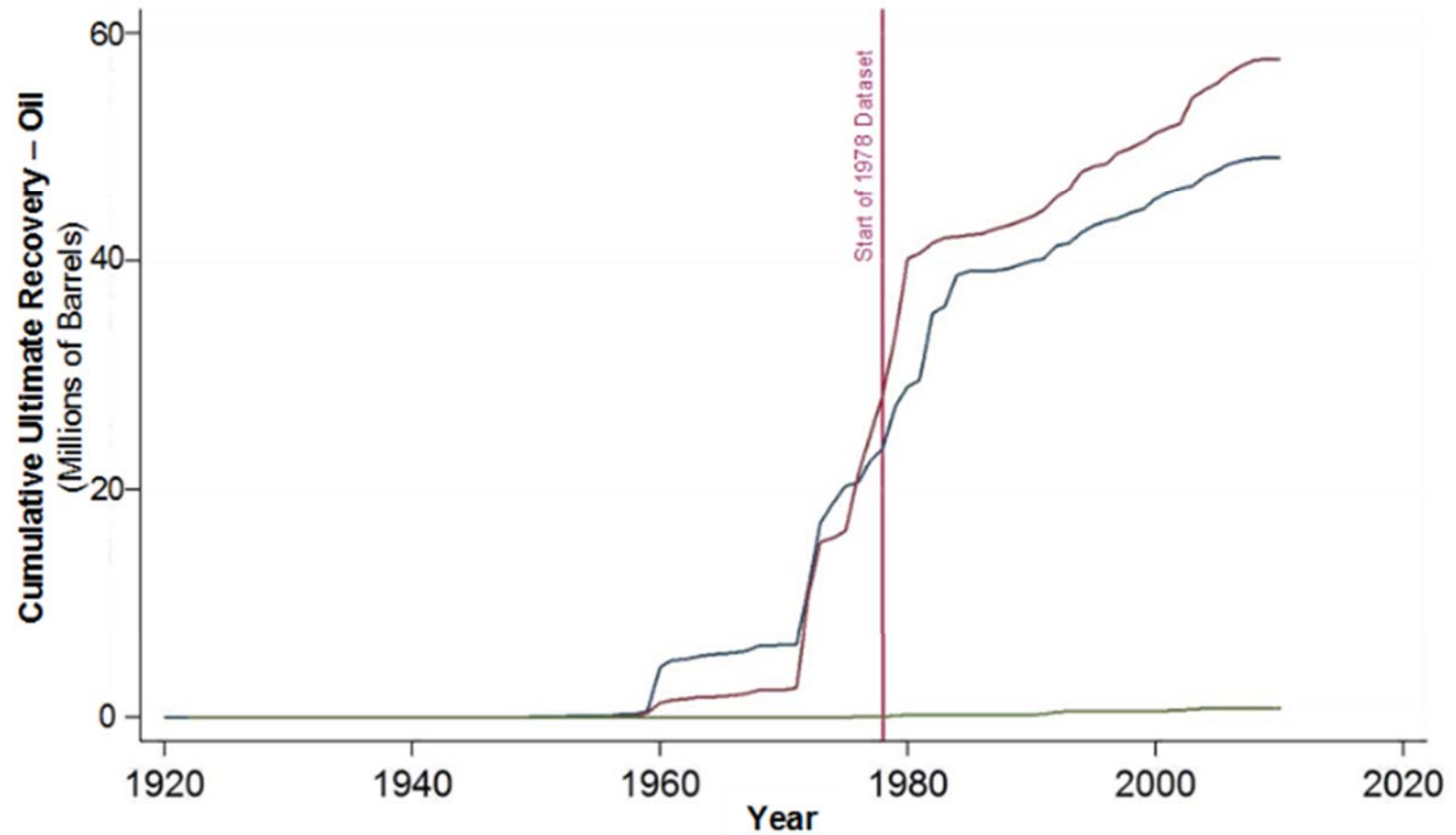
Figure 25. Cumulative Ultimate Recovery, Gas, 1950 dataset. Natural gas is plotted in billions of Mcf (Tcf). The vertical red line is a point of reference indicating the start of the 1978 dataset.
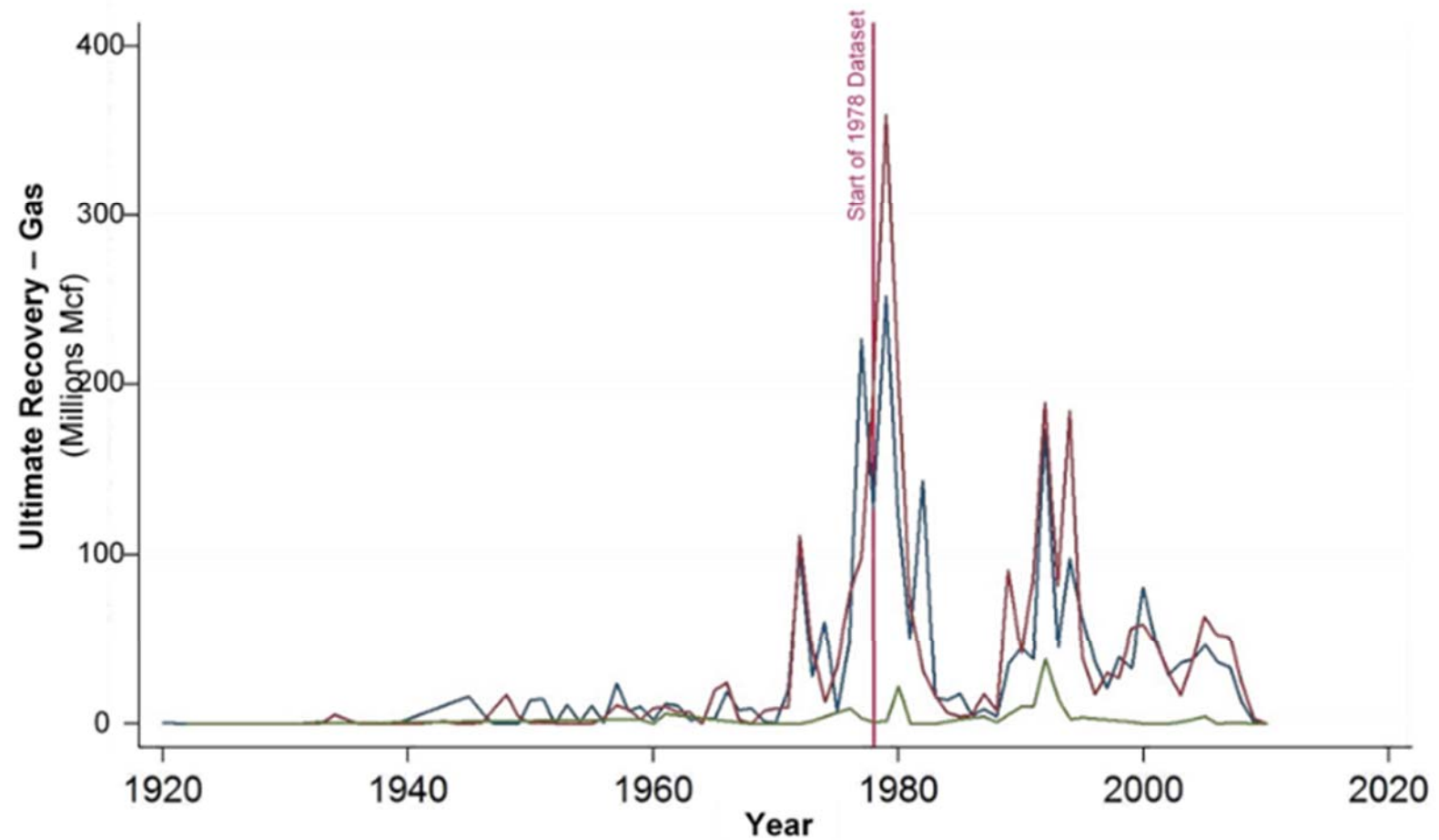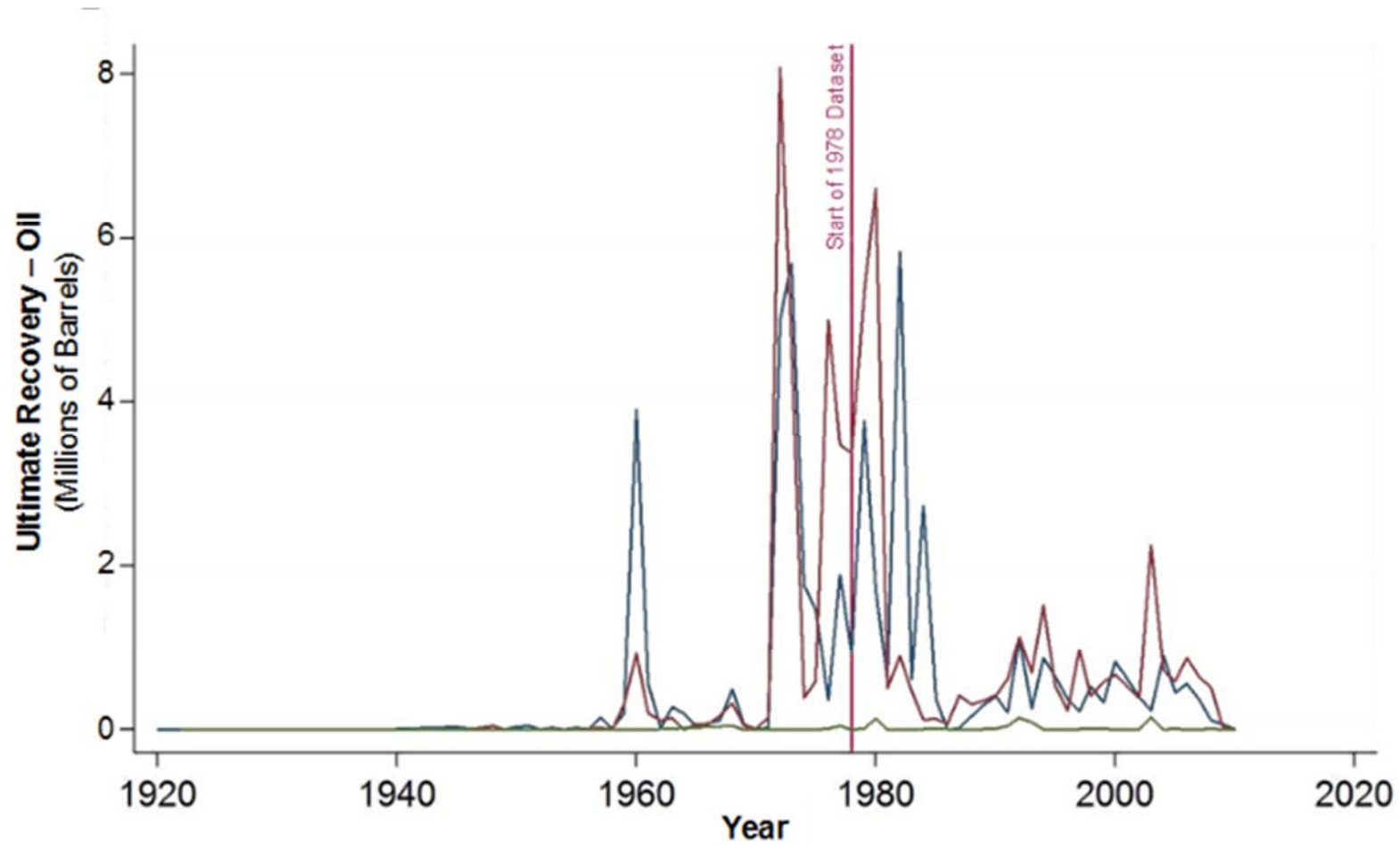
Figure 26. Ultimate Recovery, Gas, 1950 dataset.   Natural gas is plotted in millions of Mcf (Bcf). The vertical red line is a point of reference indicating the start of the 1978 dataset. All natural gas production from wells are assigned to the year the wells were drilled.

**Figure 27.** Cumulative Producing Wells, 1950 dataset.

Figure 28. Cumulative Ultimate Recovery, Oil, 1950 dataset. Crude oil is plotted in millions of barrels. The vertical red line is a point of reference indicating the start of the 1978 dataset.

Figure 29 Ultimate Recovery, Oil, 1950 dataset. Crude oil is plotted in millions of barrels. The vertical red line is a point of reference indicating the start of the 1978 dataset.
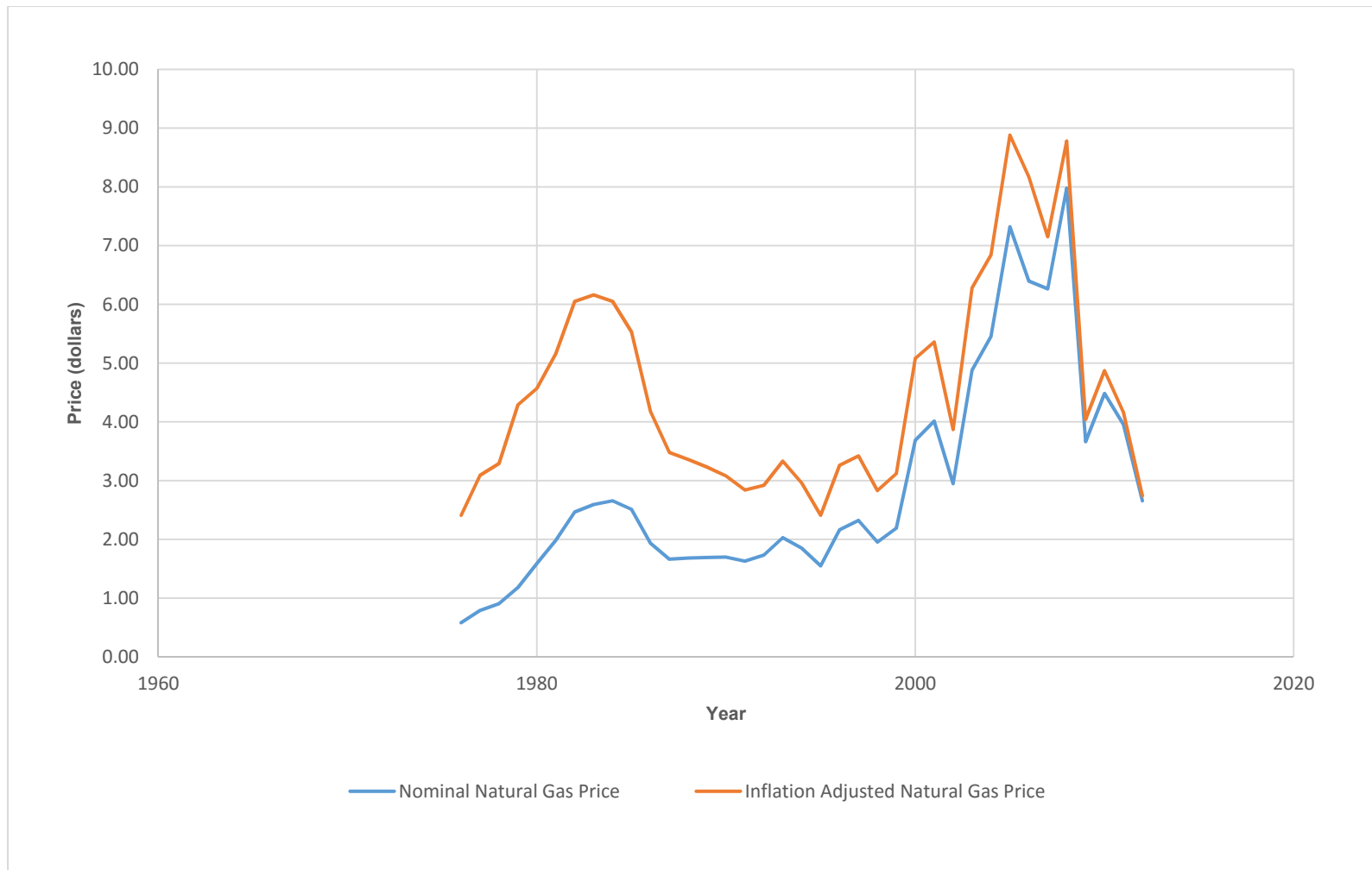
Figure 30. Nominal and inflation adjusted natural gas prices. Natural gas price and inflation adjustment data from *inflationdata.com*.
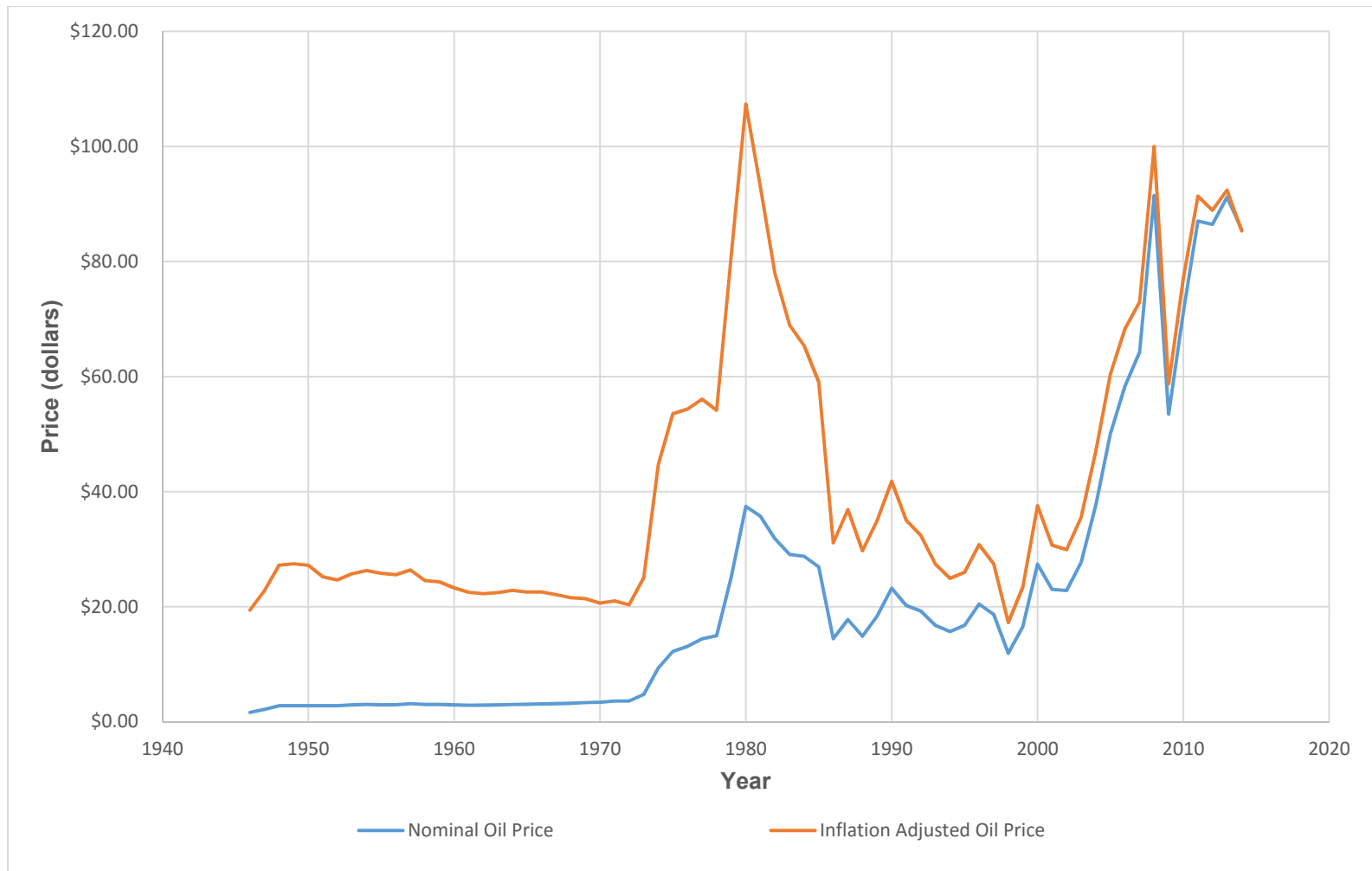
Figure 31. Nominal and inflation adjusted crude oil prices. Oil price and CPI index are from the Energy Information Administration and US Bureau of Labor Statistics.